This is a repository copy of *Local Ca2+ signals couple activation of TRPV1 and ANO1 sensory ion channels*.

White Rose Research Online URL for this paper:
http://eprints.whiterose.ac.uk/159064/

Version: Accepted Version

One-Sentence Summary: TRPV1-mediated release of ER Ca^{2+} is sufficient to activate the sensory ion channel ANO1.

Editor's Summary:
Boosting the Ca^{2+} signal for nociception

The Ca^{2+}-activated Cl^- channel ANO1 promotes nociception, the perception of pain. The nonselective cation channel TRPV1 has been proposed to be the source of Ca^{2+} that activates ANO1, but the amount of Ca^{2+} that TRPV1 allows into pain-transmitting DRG neurons is thought to be insufficient to activate ANO1. Shah et al. found that TRPV1 triggered Ca^{2+} release from the ER through an IP_3 receptor isoform. Imaging techniques showed that ANO1, TRPV1, and the IP_3 receptor clustered in close proximity to each other in pain-transmitting DRG neurons. These results provide insight into the molecular mechanisms underlying nociception.

Local Ca^{2+} signals couple activation of TRPV1 and ANO1 sensory ion channels

Shihab Shah[1], Chase M. Carver[2], Pierce Mullen[1], Stephen Milne[1], Viktor Lukacs[1], Mark S. Shapiro[2], Nikita Gamper[1,3]*

[1]School of Biomedical Science, Faculty of Biological Sciences, University of Leeds, Leeds, LS2 9JT, UK

[2]Department of Cell and Integrative Physiology, University of Texas Health San Antonio, San Antonio, TX 78229, USA

[3]Department of Pharmacology, Hebei Medical University, Shijiazhuang 050017, People's Republic of China

*Correspondence should be sent to

Nikita Gamper
School of Biomedical Science,
Faculty of Biological Sciences,
University of Leeds, Leeds, LS2 9JT, UK
+44(0)1133437923
n.gamper@leeds.ac.uk

Abstract

ANO1 (TMEM16A) is a Ca^{2+}-activated Cl^- channel (CaCC) expressed in peripheral somatosensory neurons that are activated by painful (noxious) stimuli. These neurons also express the Ca^{2+}-permeable channel and noxious heat sensor TRPV1, which can activate ANO1. Here, we revealed an intricate mechanism of TRPV1-ANO1 channel coupling in rat dorsal root ganglion (DRG) neurons. Simultaneous optical monitoring of CaCC activity and Ca^{2+} dynamics revealed that the TRPV1 ligand capsaicin activated CaCCs. However, depletion of endoplasmic reticulum (ER) Ca^{2+} stores reduced capsaicin-induced Ca^{2+} increases and CaCC activation, suggesting that ER Ca^{2+} release contributed to TRPV1-induced CaCC activation. ER store depletion by plasma membrane-localized TRPV1 channels was demonstrated with an ER-localized Ca^{2+} sensor in neurons exposed to a cell-impermeable TRPV1 ligand. Proximity ligation assays established that ANO1, TRPV1 and the IP_3 receptor IP_3R1 were often found in close proximity to each other. Stochastic optical reconstruction microscopy (STORM) confirmed the close association between all three channels in DRG neurons. Together, our data reveal the existence of ANO1-containing multi-channel nanodomains in DRG neurons and suggest that coupling between TRPV1 and ANO1 requires ER Ca^{2+} release, which may be necessary to enhance ANO1 activation.

Introduction

Ca^{2+} activated Cl^- channels (CaCCs) are important regulators of epithelial transport, smooth muscle contraction and neuronal excitability (reviewed in (1-4)). The molecular identity of CaCCs remained elusive until 2008, when 3 groups identified ANO1 (TMEM16A), a member of the anoctamin (TMEM16) family of transmembrane proteins, as a bona fide CaCC (5-7). Functional expression of ANO1 has been confirmed in peripheral damage-sensing (nociceptive) neurons (7-10). In contrast to most adult CNS neurons, peripheral somatosensory neurons accumulate relatively high intracellular $[Cl^-]_i$, sufficient to maintain their Cl^- equilibrium potential (E_{Cl}) at voltages more positive than the threshold for action potential firing (8, 11). Therefore, activation of ANO1-mediated CaCCs in these cells can increase excitability and trigger or potentiate nociception. Furthermore, the Na^+, K^+ and Cl^- cotransporter NKCC1 is upregulated in sensory neurons during nerve injury (12), which leads to further Cl^- accumulation and potentially even greater excitatory effects of ANO1 currents.

ANO1 channels possess an intrinsically low Ca^{2+} sensitivity with an EC_{50} in the range of 2-5 µM at -60 mV (7, 13). This low sensitivity may be due to the unusual location of the Ca^{2+} binding site of ANO1, which localizes to a domain between the α6 and α8 transmembrane helices situated within the lipid bilayer (14). The Ca^{2+} sensitivity of ANO1 is voltage dependent such that it increases with depolarization (13, 15); for example, an EC_{50} of 0.4 µM is measured at +100 mV. Nevertheless, at the resting membrane potential of sensory neurons of ~-60 mV (16-18), $[Ca^{2+}]_i$ of >1-2 µM is required to activate ANO1. Global Ca^{2+} levels in the cytosol do not normally reach micromolar concentrations, and therefore, to enable reliable ANO1 activation, localized, high-intensity Ca^{2+} signals are required (1, 19-21). Intriguingly, in sensory neurons from dorsal root ganglion (DRG) neurons, ANO1 is found in close proximity to G protein coupled receptors (GPCRs), such as the bradykinin (BK) B_2 receptor (B_2R) and the protease activated receptor-2 (PAR2) on the plasma membrane (PM), and physically coupled with endoplasmic reticulum (ER) localized IP_3 receptors (IP_3Rs), forming a junctional ER-PM complex (19).

We have shown that upon stimulation of such $G_{q/11}$-coupled GPCRs (GqPCRs), IP_3 generation activates IP_3Rs, which, in turn, leads to Ca^{2+} release from the ER and ANO1 activation. Due to the proximity between the components of the junctional complex, local Ca^{2+} elevations, which reach up to 50-75 µM at the mouth of IP_3R channel (22, 23), are sufficient to enable ANO1 activation (19). BK, proteases and other relevant GPCR ligands are released upon tissue inflammation and contribute to inflammatory pain and itch, in part through the GPCR-induced activation of ANO1/CaCCs and depolarization of nociceptive afferents (8, 24-27). Localization of ANO1 channels to ER-PM junctional nanodomains may also serve the function of shielding ANO1 channels from activation by other, non-colocalized Ca^{2+} signals, such as those generated by voltage-gated Ca^{2+} channels during action potential firing (1, 19, 28).

ANO1 in DRG neurons can also be activated by noxious heat at a similar temperature range to the 'canonical' noxious heat sensor TRPV1 (9, 10). In addition, TRPV1 is another major mediator of inflammatory pain, and activation of TRPV1 channels is sensitized by BK and PAR2 (25, 29). Furthermore, opening of TRPV1 channels activates ANO1 in sensory neurons (10). The latter study suggested that ANO1 and TRPV1 are directly coupled, with Ca^{2+} entry through TRPV1 providing the local Ca^{2+} elevation that allows ANO1 activation (10). Notably, the Ca^{2+} influx through TRPV1 amounts to no more than ~10% of the total TRPV1 cation current (30). On the other hand, TRPV1 activates Ca^{2+}-sensitive phospholipase C (PLCδ) and induces Ca^{2+} release from the ER in the absence of prior stimulation of G_qPCRs (31). Thus, the question arises: Is direct Ca^{2+} influx through the TRPV1 channel pore sufficient to fully activate ANO1 in sensory neurons or are other Ca^{2+} sources also involved or obligatory? Using live-imaging approaches, patch-clamp electrophysiology, proximity ligation and a super-resolution microscopy method, we demonstrated that a substantial fraction of ANO1 and TRPV1 channels were found in junctional nanodomains in small-diameter nociceptors and that TRPV1-mediated Ca^{2+} release from ER-resident IP_3Rs was a major factor in functional TRPV1-ANO1 coupling.

Results

Single-cell fluorescence imaging can measure currents through CaCCs

Imaging of halide-sensitive enhanced yellow fluorescent protein (EYFP) mutants has been previously used to monitor Cl^- channel activity (32-34). The method is based on the permeability of most anion channels to iodide ions (I^-), which, when added to the extracellular solution, quenches EYFP fluorescence in a manner dependent on anion channel opening. However, previous applications of this technique, including a single-cell approach developed by us (19), do not allow correlation of intracellular Ca^{2+} dynamics with I^- influx. Furthermore, the agonist-independent quenching complicates quantification and masks the response obtained by agonists. Here we developed a triple-wavelength imaging approach to simultaneously monitor halide-sensitive EYFP quenching and ratiometric fura-2 Ca^{2+} imaging (**Fig. 1A**). DRG neurons abundantly express $GABA_A$ Cl^- channels (35-37); thus, we used GABA responses from cultured rat DRG neurons transfected with the halide-sensitive mutant EYFP H148Q/I152L (EYFP-QL) to optimize the extracellular I^- concentration and minimize agonist-independent quenching (**Fig. 1B-E**). Equimolar replacement of 5-30 mM NaCl with NaI revealed that 5 mM NaI offered the lowest rate of agonist-independent EYFP-QL quenching while providing sufficient dynamic range for the reliable detection of Cl^- channel opening.

We then performed simultaneous halide and Ca^{2+} imaging of DRG neurons transfected with EYFP-QL and loaded with fura-2AM. B_2R receptors were stimulated by bath-application of BK (250 nM) in the presence of 5 mM NaI while performing triple-wavelength excitation (340/380/488nm). Consistent with our previous study (19), BK induced robust transient $[Ca^{2+}]_i$ rises which were temporally correlated with the EYFP-QL fluorescence quenching (**Fig. 2A, B**). In contrast to the Ca^{2+} rises, which were transient in nature, the EYFP-QL quenching did not normally recover within the period of observation (reflecting that once I^- is taken up by a cell during CaCC activation, it is not easily extruded under our experimental conditions). The mean amplitude of the peak fura-2 Ca^{2+} signal ($\Delta R/R_0$) and the mean drop in the normalized EYFP-QL fluorescence ($\Delta F/F_0$) induced by BK are shown in **Fig. 2C** (left).

To confirm that this quenching was indeed mediated by ANO1 and not another Cl$^-$ channel flux, transfected cells were preincubated and perfused with two ANO1 inhibitors, T16A-inhA01 and Ani9 (38). In the presence of T16A-inhA01 (50 μM), EYFP-QL quenching induced by BK was abolished despite the presence of Ca^{2+} transients (**Fig. 2C**). Ani9 (500 nM) also inhibited BK-induced quenching, although to a lesser extent. The BK-induced [Ca^{2+}]$_i$ rises were smaller in the presence of both ANO1 inhibitors, compared to control conditions (**Fig. 2C**). This observation is consistent with the hypothesis that ANO1 is not only a target of the Ca^{2+} signals, but may also facilitate ER Ca^{2+} release because of structural interactions between the PM and the ER (28). Hence, both T16A-inhA01 and Ani9 may interfere with this process. However, BK application still induced measurable rises in [Ca^{2+}]$_i$ in the presence of T16A-inhA01 and Ani9, whereas EYFP-QL quenching was either abolished (T16A-inhA01) or significantly reduced (Ani9). This indicates that our imaging approach allows reliable, all-optical measurement of ANO1-mediated CaCCs and concurrent Ca^{2+} dynamics in individual DRG neurons.

TRPV1-ANO1 coupling requires Ca^{2+} release from the ER

ANO1 activation is coupled to intracellular Ca^{2+} release from IP$_3$Rs in DRG neurons (19). To confirm this coupling using our imaging approach, BK was applied in the absence of Ca^{2+} in the extracellular bath solutions (**Fig. 2D**). The amplitude of EYFP-QL quenching was not affected by the removal of extracellular Ca^{2+} (**Fig. 2E**), despite a significantly lower induced [Ca^{2+}] rise, compared to control conditions. This finding suggested that even though Ca^{2+} influx through PM Ca^{2+} channels contributed to the global Ca^{2+} rises induced by BK (8), it was the ER Ca^{2+} release that specifically activated ANO1/CaCC following B$_2$R activation. Indeed, as shown previously (19), Ca^{2+} influx through voltage-gated Ca^{2+} channels (VGCCs) is poorly-coupled to ANO1 activation in DRG neurons. To verify this finding using our imaging approach, we stimulated Ca^{2+} influx through VGCCs by depolarizing neurons with an extracellular solution containing 50 mM KCl (**fig. S1A, B**). The majority (15/23 or 65%) of DRG neurons did not respond to 50 mM K$^+$ with any measurable EYFP-QL quenching, despite strong rises in [Ca^{2+}]$_i$. The remaining 35% (8/23) neurons did display quenching (**fig. S1A, B**). However,

significant EYFP-QL quenching induced by 50 mM KCl was observed in some DRG neurons in the absence of extracellular Ca^{2+} as well (**fig. S1C, D**). Because $[Ca^{2+}]_i$ rises were not recorded under these conditions, we conclude that depolarization-induced quenching observed in the minority of DRG neurons was likely not CaCC-related. In summary, our data (**Fig. 2, A to E** and **fig. S1, A to D**) established a reliable optical approach for measuring CaCC activation in DRG neurons and confirmed preferential coupling of ANO1/CaCC to IP_3R-mediated Ca^{2+} release from the ER rather than Ca^{2+} influx through PM Ca^{2+} channels in DRG neurons.

TRPV1 activation in DRG neurons and in heterologous expression systems results in activation of ANO1; furthermore, ANO1 potentiates TRPV1-induced depolarization in vitro and the sensory response to heat in vivo (10). ANO1 is itself a heat-sensitive channel, with its thermo-sensitivity modulated by Ca^{2+} (9). Moreover, both ANO1 and TRPV1 channels are targeted by BK signals (8, 19, 39). Thus, elucidating the relationships between these two channels may reveal aspects of thermal sensitivity and inflammatory pain mechanisms. Takayama and colleagues suggested that TRPV1 and ANO1 interact physically and that Ca^{2+} influx through TRPV1 is the main mechanism of coupled ANO1 activation. However, TRPV1 is a nonselective cation channel and under physiological conditions conducts mostly Na^+ currents with Ca^{2+} influx contributing only 7-10% of the overall current (30). On the other hand, TRPV1 activation in DRG neurons induces PLC activation and ER Ca^{2+} release (31). Given the coupling of ANO1 to ER-released Ca^{2+}, we used our optical recording approach to test if this Ca^{2+} source contributed to TRPV1-ANO1 coupling as well. TRPV1 activation with 1 μM capsaicin induced significant EYFP-QL quenching (**Fig. 3A, B**), which correlated with intracellular Ca^{2+} rises (**Fig. 3A**). Both the capsaicin-induced EYFP-QL quenching and Ca^{2+} transients were comparable to those induced by BK (**Fig. 3C**).

Next, we tested if Ca^{2+} release from the ER contributed to TRPV1-induced ANO1 activation. As a first step, we measured capsaicin-induced Ca^{2+} transients in untransfected DRG neurons after ER store depletion produced by inhibition of the sarco/endoplasmic reticulum Ca^{2+}-ATPase by either thapsigargin

(TG; 1 μM) or cyclopiazonic acid (CPA;1 μM; **Fig. 3D**, **fig. S2A**). Consistent with a previous report (31), Ca^{2+} transients were significantly reduced in the presence of both drugs. However, after removal of Ca^{2+} from the extracellular bath solutions, capsaicin still produced Ca^{2+} signals (**Fig. 3D**, **fig. S2A**). These were significantly smaller as compared to control conditions, yet clearly identifiable. These initial experiments indicate that TRPV1 can induce sizeable Ca^{2+} release from the internal stores, which contributes approximately one half of the global Ca^{2+} signal measured by fura-2.

Next, we used triple-wavelength imaging to investigate the effect of store depletion on ANO1 activation, as measured with EYFP-QL quenching. Depletion of ER Ca^{2+} stores with TG reduced not only Ca^{2+} transients after capsaicin application but also EYFP-QL quenching (**fig. S2B, C**). We also applied capsaicin in Ca^{2+}-free extracellular solution and using our triple wavelength imaging approach determined that both Ca^{2+} transients and significant EYFP-QL quenching were still present (**fig. S3A, B**). These results provide further support for our proposal that CaCC activation through TRPV1 requires the ER component. We also tested whether ER Ca^{2+} 'leak' could induce CaCC activation in our experimental setup. Acute application of TG to EYFP-QL-transfected DRG neurons produced Ca^{2+} transients and some EYFP-QL quenching (**fig. S3C, D**).

To further probe the relationship between TRPV1 activation, ER Ca^{2+} release and ANO1 activation, we expanded our imaging approach to enable simultaneous but separate monitoring of Ca^{2+} levels in the ER and cytosol together with EYFP-QL quenching. To allow ER Ca^{2+} monitoring, we used the ER-targeted, Ca^{2+} sensing protein red-CEPIA (40). CEPIA fluorescence is reduced as Ca^{2+} is released from the ER. We transfected DRG cultures with both EYFP-QL and red-CEPIA and also loaded cells with fura-2AM, thereby allowing us to concurrently monitor CaCC activity, ER Ca^{2+} levels and cytosolic Ca^{2+} dynamics, respectively. A quadruple-wavelength (340/380/488/560nm) imaging protocol was utilized to simultaneously image all fluorophores in the experiments. Application of capsaicin produced Ca^{2+} transients and evoked significant EYFP-QL quenching but also resulted in a reduction in red-CEPIA fluorescence which indicates Ca^{2+} moving out of the ER after TRPV1 activation (**Fig. 3E, F**). This

experiment also directly demonstrated good temporal correlation between ER Ca^{2+} depletion, cytosolic Ca^{2+} elevation, and CaCC activation.

To validate our imaging results, we made whole-cell patch clamp recordings from cultured DRG neurons using physiological bath and internal pipette solutions. Application of capsaicin elicited robust inward currents (**Fig. 4A**). The current amplitude and kinetics of the response varied substantially; therefore, we quantified the area under the curve (A.U.C.) as a readout of TRPV1 activation. To test the contribution of ANO1 to this current, DRG neurons were preincubated with Ani9 (500 nM; **Fig. 4A**). In the presence of Ani9, the capsaicin-induced A.U.C. was significantly reduced, which was consistent with a previous study (10). To test if Ca^{2+} release from the ER was necessary for TRPV1-coupled ANO1 activation in DRG neurons, we pretreated neurons with TG (1 μM), which significantly reduced the capsaicin-induced A.U.C. (**Fig. 4B, C**). In the presence of TG, the majority of responses to capsaicin were lower compared to those evoked in control conditions (**Fig. 4B**, black trace; **Fig. 4C**). However, in 5 TG-treated neurons, capsaicin-induced responses were within the range of the average capsaicin response under control conditions. (**Fig 4B**, red trace; **Fig. 4C**). These results suggested three conclusions. First, ANO1-mediated Cl^- current contributed substantially to the macroscopic currents induced in DRG neurons by capsaicin. Second, TRPV1-induced release of Ca^{2+} from the ER contributed substantially to TRPV1-coupled ANO1 activation in the majority of DRG neurons. Third, in some neurons, TRPV1-mediated Ca^{2+} influx was sufficient to induce strong ANO1 activation. The latter observation also argues against the possibility that TG directly interferes with TRPV1 function.

TRPV1-mediated Ca^{2+} release from the ER requires crosstalk between plasmalemmal TRPV1 and PLC

One important question that needed to be addressed was the manner in which capsaicin activated ER Ca^{2+} release. The two most likely scenarios suggested in the literature are activation of PLCs that cleave phosphatidylinositol 4,5-bisphosphate (PIP_2) to produce IP_3, which in turn, induces Ca^{2+} release through IP_3Rs in the ER (41), and direct activation of ER-localized TRPV1 channels by capsaicin (42). To

differentiate between the above mechanisms, we used two approaches. First, we performed fluo-4- Ca^{2+} imaging in DRG neurons treated with capsaicin after preincubation with (and in the presence of) ruthenium red (RR; 10 μM), a cell-impermeable TRPV1 blocker (**Fig. 5A, B**). Without access to the cytosol, RR should not inhibit putative ER-localized TRPV1 channels; therefore, capsaicin responses in the presence of this TRPV1 blocker could be attributed to this subset of channels (or any other intracellular TRPV1 channel pool). There was generally no response to capsaicin in the presence of RR (**Fig. 5A, B**). Upon wash out of RR and with capsaicin still present, Ca^{2+} responses were routinely recorded, suggesting that capsaicin did not induce noticeable Ca^{2+} transients through putative ER-resident TRPV1 channels in the majority of DRG neurons under our experimental conditions. Of 38 neurons that responded to capsaicin upon RR washout, only 4 cells produced discernable Ca^{2+} transients in the presence of RR and capsaicin. To specifically probe ER-Ca^{2+} release by TRPV1 activation, we performed imaging in DRG neurons expressing green-CEPIA to enable direct monitoring of ER Ca^{2+} levels. Capsaicin application produced significant ER-depletion only after RR washout (**Fig. 5 C, D**).

Second, we utilized a cell-impermeable TRPV1 ligand to specifically activate PM-resident TRPV1 channels while avoiding activation of intracellular TRPV1s. Double-knot toxin (DkTx) is a vanillotoxin from the Chinese bird spider (Ornithoctonus huwena) which activates TRPV1 by binding to its extracellular outer pore turret (43-45). Here we used a single-knot derivative of DkTx, K2, which activates TRPV1 with improved efficacy (46). Both capsaicin and K2 (30 μM) evoked comparable Ca^{2+} transients in DRG neurons (**Fig. 5E, F**). In the absence of Ca^{2+}, K2 still induced cytosolic Ca^{2+} transients (**Fig. 5F** and **fig. S4**). Finally, DRG cultures were transfected with red-CEPIA and K2 was applied to test whether Ca^{2+} release from the ER could be detected. K2 induced significant reduction in CEPIA fluorescence in 8/12 neurons tested (**Fig. 5G, H**). The data obtained with both a cell-impermeable TRPV1 agonist and a cell-impermeable antagonist suggested that activation of PM-localized TRPV1 channels

was indeed capable of inducing Ca^{2+} release from the ER. Contribution of putative ER-localized TRPV1 channels to the capsaicin-induced cytosolic Ca^{2+} signal in DRG neurons appeared to be negligible.

The alternative possibility is that TRPV1 activation in DRG neurons was coupled to PLC activation and subsequent Ca^{2+} mobilization (31). To test this possibility, we transfected DRG neurons with an optical PIP_2 reporter, GFP-tagged plextrin homology domain of PLCδ (PLCδ-PH-GFP) and monitored its translocation from the membrane to cytosol following the capsaicin application as a measure of PIP_2 hydrolysis by PLC (47). Application of capsaicin (1 µM) induced translocation of PLCδ-PH-GFP from the PM to the cytosol (**fig. S5A, B).** Translocation was recorded even in the in the absence of extracellular Ca^{2+}, albeit to a smaller extent (**fig. S5B**). Both of these findings are consistent with the previous report (31) and with our K2 experiments.

ANO1, TRPV1 and IP_3R cluster at ER-PM junctions

Our results above suggested that there were functional interactions between ANO1, TRPV1 and IP_3Rs that allowed TRPV1 to activate ANO1 through IP_3R-mediated Ca^{2+} release, supplementing the relatively small Ca^{2+} influx through TRPV1 itself (30). For this mechanism to occur, there must be close proximity between these channel proteins. Previous work suggests that at least some ANO1 channels in DRG neurons reside at ER-PM junctions (1, 19), which are sites for intracellular information transfer where two membrane types come into very close juxtaposition (~15 nM) (48). At these sites ANO1 channels may physically interact with the IP_3Rs (19, 49). To test if all three proteins were found in close association, we first utilized a proximity ligation assay (PLA) which detects two proteins that are closer than 30-40 nm from each other by manifesting characteristic 0.5-1 µm fluorescent puncta (50, 51). All antibodies used for PLA have been previously validated extensively by us in sensory neurons (19, 52).

Specific PLA signals indicating close proximity were detected for TRPV1-ANO1 (**Fig. 6A**), ANO1-IP_3R1 (**Fig. 6B**) and TRPV1-IP_3R1 (**Fig. 6C**) protein pairs. A particularly high concentration of puncta per neuron was observed for the TRPV1-ANO1 pair (**Fig. 6D**). Positive PLA controls using two primary ANO1 antibodies raised in rabbit and goat and corresponding secondary PLA probes displayed robust

puncta (**fig. S6A**). When only the rabbit primary antibody was used with both secondary probes, no signal was detected (**fig. S6B**). No puncta were observed when PLA was performed between IP$_3$R1 and CD71 (also known as the transferrin receptor) (**fig. S7A**), a non-raft plasmalemmal protein (19, 53) that is not expected to co-localize with the members of the ANO1 junctional complex (19). These controls confirm PLA specificity in our experimental settings. Together, these data established that ANO1, TRPV1 and IP$_3$R1 in DRG neurons often are found in close proximity. Of the three pairs tested, TRPV1-ANO1 complexes were more easily detectable, perhaps reflecting the PM residence of these proteins, whereas ANO1-IP$_3$R1 and TRPV1-IP$_3$R1 interactions exist across the ER-PM junction.

STORM super-resolution microscopy allows direct visualization of individual ANO1-TRPV1-IP$_3$R complexes

To further probe the existence of multi-channel complexes suggested by the above data with greater precision, we employed multi-wavelength super-resolution microscopy that can detect individual protein molecules in the membrane of fixed primary cells. Stochastic optical reconstruction microscopy (STORM) (54, 55) allows multiple fluorophore excitation and detection using visible light, enabling localization of individual proteins, or complexes within a lateral resolution of less than 50 nm (52). Our previous work (52) describes in detail the extensive controls performed for such multi-wavelength STORM and the analysis paradigms that we have developed. The traditional STORM approach incorporates different "activator" fluorescent dyes (in this work we used Alexa Fluor 405, Cy2, and Cy3, excited at either 405 nm, 488 nm or 561 nm, respectively) that excite a common "reporter" fluorescent dye (for example, Alexa Fluor 647), that are both conjugated to secondary antibodies to identify which activator dye is the source of the excitation signal through tight temporal correlation. Each protein of interest is first labeled with appropriate primary antibodies that we have validated previously (19, 52). Because each secondary antibody is specific to the species of a corresponding primary antibody (mouse, rabbit, goat), we can simultaneously visualize individual complexes containing up to three different proteins. Control experiments by our group have shown a single tetrameric ion channel (such as voltage-

gated K^+ channel or a TRP channel) to be represented by a cluster of labeled "centroids" (single-molecule localizations) with a radius of ~30-50 nm, in which a single type of protein is represented by a cluster of densely proximal, like-colored centroids (52). Complexes containing two or three types of physically associated proteins are represented by clusters of centroids of two or three colors, with a slightly greater radial "footprint" of the antibody-dye label (52). Each standalone cluster of centroids of a single color represents a protein or a complex (such as a multimeric ion channel), recognized by a single type of a primary antibody. Clusters of centroids are objectively identified with a DBSCAN algorithm based on the original STORM localization data, which we previously described. Differential bleaching kinetics of Cy2 and Cy3 and Alexa Fluor 405 (**fig. S8**) was corrected.

First, we used STORM to probe for the same combinations of protein complexes tested in the PLA experiments (TRPV1-ANO1, ANO1-IP$_3$R1 and TRPV1-IP$_3$R1; **Fig. 7A, B, C**). Clusters of centroids representing individual ANO1, TRPV1 and IP$_3$R1 channels were detected in each corresponding experiment and, as expected, a fraction of these centroid clusters were co-mingled within a combined radius of <120 nm, indicating close association. Even when in tight proximity (<100 nm), the footprint of each channel protein, as labeled by the STORM-visualized antibody/dyes could be individually resolved from the associated, coupled protein (**Fig. 7A, B, C**). Of the total detected clusters of centroids for TRPV1 and ANO1, 74.1 ± 6.5% were identified as co-localized channels based on our analysis paradigm (52) (**Fig. 7D**). The observed overlap of the two channels (as represented by their respective like-colored centroid clusters) in 2D space in the STORM image was usually not complete, suggesting discrete channels that were physically coupled in the PM within very close proximity. Non-colocalized ANO1 (2.3 ± 0.5%) and TRPV1 channels (23.5 ± 6.4%) were also detected which were a lower fraction compared to the co-localized population (**table S1**).

In our experiments, STORM was performed on a microscope platform similar to that of total internal reflection microscopy (TIRF), in which illumination of cells is typically restricted to <400 nm from the surface of the glass, with the bulk of the light internally reflected (56, 57). In STORM, the angle of the

laser light can be altered so that the illumination is not fully internally reflected, but adjusted so it is sufficiently oblique to penetrate up to ~1 μm, allowing illumination of the cytosol or organelles (such as the ER membrane) within 1 μm of the plasma membrane. Thus, we used STORM to examine the presence of complexes containing individual TRPV1 or ANO1 channels in the PM, and closely proximal to ER-resident IP$_3$Rs. In double-labeling of ANO1 and IP$_3$R1 under STORM, we detected co-localized ANO1-IP$_3$R1 complexes, represented by clusters of centroids of two colors, accounting for $54.2 \pm 4.3\%$ of all detected centroid clusters observed in DRGs (**Fig. 7E**). Clusters of centroids of a single color, representing individual ANO1 channels or IP$_3$R1s comprised $23.8 \pm 4.0\%$ and $22.0 \pm 8.1\%$ of all clusters, respectively. We also probed for complexes containing TRPV1 and IP$_3$R1, and found co-localization of the two proteins, accounting for $51.8 \pm 4.0\%$ of detected clusters (**Fig. 7F**). Individual TRPV1 and IP$_3$R1 clusters amounted to $34.0 \pm 4.0\%$ and $14.1 \pm 0.8\%$ of total clusters, respectively (**table S1**). As with the PLA data, the fraction of total TRPV1-ANO1 complexes per cell was more abundant as compared to complexes containing ANO1-IP$_3$R1 or TRPV1-IP$_3$R1. Although this cross-comparison of protein pairs (both by STORM and PLA) suggests the co-localization of ANO1, TRPV1 and IP$_3$R1 that we can visualize, it does not provide quantitative evidence for the relative abundance of individual pairs, because the primary antibody affinities to their respective epitopes are not uniform and cannot be meaningfully normalized.

Because the PLA approach is limited to the detection of protein pairs only, we performed triple-labeled STORM imaging to probe for complexes containing all three proteins (ANO1, 405/647; TRPV1, 488/647; IP$_3$R1, 561/647; **Fig. 8A, B, C**). The fraction of ANO1, TRPV1, and IP$_3$R1 detected as co-localized together was $40.2 \pm 0.2\%$, which accounted for the majority of the co-localizations compared to the pairs of only TRPV1-ANO1 ($15.7 \pm 1.6\%$), ANO1-IP$_3$R1 ($4.2 \pm 0.04\%$), and TRPV1-IP$_3$R1 ($6.4 \pm 1.6\%$) without a third protein observed (**table S1**). The ANO1-IP$_3$R1-only and TRPV1-IP$_3$R1-only populations were small and under the noise threshold of interactions detectable under STORM that we

previously determined. This "noise threshold" was experimentally determined as ~10% of total clusters (based on spurious interactions of KCNQ2 and KCNQ4 channels) and in which the binned cluster radii are consistently less than 1% of the total fraction of clusters (52). Clustering between IP$_3$R1 and CD71 amounted to $10.6 \pm 1.6\%$ of total clusters (**fig. S7B**), confirming the stringency of our threshold criteria and agreeing with the PLA results (**fig. S7A**).

In triple-labeled cells, TRPV1-ANO1 co-localizations remained prevalent, consistent with the large number of physical interactions of these two PM proteins in the double-label STORM experiments. However, the mean radius and centroid density of the ANO1-TRPV1-IP$_3$R1 clusters were significantly larger than these of the TRPV1-ANO1 (no IP$_3$R1) clusters, presumably due to the addition of the IP$_3$R1s (**tables S2 and S3**). This is important when comparing these data to the double-labeled STORM experiments, in which the cluster populations of co-localized pairs of proteins were similar in size and centroid density (**tables S2 and S3**). Based on the proportion of complexes, we can surmise that ANO1 and TRPV1 are more likely to cluster in the presence of co-localized IP$_3$R1, as evident in the significantly greater number of triple-color clusters including IP$_3$R1s.

Discussion

In this work, we investigated the mechanism coupling TRPV1 channel opening with the activation of ANO1/CaCC in small-diameter (presumed nociceptive) DRG neurons. In the original report of TRPV1-ANO1 interactions, Takayama and colleagues put forward the most straightforward explanation for the mechanism of coupling: Opening of the TRPV1 channel pore delivers a sufficient amount of Ca^{2+} to directly activate co-localized ANO1 channels (10). Yet, several considerations compelled us to look beyond Occam's razor. First, the affinity of Ca^{2+} ions for ANO1 at negative voltages is low (2-5 μM (7, 13)). Second, the Ca^{2+} current fraction amounts to no more than 10% of the macroscopic TRPV1 current under physiological conditions (30). This means that at similar whole-cell current amplitudes (at typical voltages during stimulation), the TRPV1-mediated Ca^{2+} influx would only deliver a fraction of Ca^{2+} ions to the cytosol as compared to those through VGCCs; however, even the latter source alone is not sufficient to produce strong ANO1 activation in DRG neurons ((19); present study). Third, evidence exists suggesting that the ER store refilling Ca^{2+} release activated channels (CRAC) in Xenopus oocytes are indirectly coupled to ANO1 activation. Ca^{2+} entering the cytosol through CRAC is not sufficient to activate ANO1 due to lack of close proximity between the ANO1 and CRAC. Instead, this cytosolic Ca^{2+} is first pumped into the ER by the SERCA pump and then released through the IP3Rs onto the juxtaposed ANO1 channels to produce activation of the latter (58). Finally, TRPV1 activates Ca^{2+}-sensitive PLCδ and induces subsequent Ca^{2+} release from the ER through IP3Rs in DRG neurons and expression systems (31, 59). Thus, there might be both the need and a mechanism for more focused delivery of Ca^{2+} to ANO1 channels to ensure robust TRPV1-ANO1 coupling.

Here, using various approaches, we investigated the mechanism of localized Ca^{2+} signals linking ANO1 channel activation to TRPV1 in DRG neurons. First, we confirmed previous observations regarding the coupling of ANO1 to Ca^{2+} sources in DRG neurons: ANO1 can be reliably activated by G_qPCR-induced Ca^{2+} release from the ER (**Fig. 2, A, D, E** and (7, 19, 49)) and by Ca^{2+} transients

downstream of TRPV1 activation (**Fig. 3A-F** and (10)), whereas Ca^{2+} influx through VGCCs is poorly

coupled to ANO1 activation (**fig. S1A-B** and (19)).

We also discovered that the predominant source of Ca^{2+} for TRPV1-coupled ANO1 activation is, as

in the case with G_qPCRs, release of Ca^{2+} from the ER. Indeed, ER store depletion significantly reduced

capsaicin-induced Ca^{2+} transients (**Fig. 3D**) and CaCC activation (**Fig. 4B** and **fig. S2B-C**). In support

of the conclusion that TRPV1 is capable of inducing robust Ca^{2+} release from the ER, we demonstrated

that capsaicin-induced depletion of ER $Ca^{2+}$was temporally correlated with the rise in cytosolic Ca^{2+}

levels and CaCC activation in DRG neurons (**Fig. 3E-F**). Capsaicin still produced small Ca^{2+} transients

in the absence of extracellular Ca^{2+} (**Fig. 3D, fig. S2A**), which could be explained by the presence of

some functional TRPV1 channels within the ER membrane (60). Such a mechanism could also contribute

to coupling of ER Ca^{2+} release to ANO1 activation. However, employing a cell membrane impermeable

manipulators of TRPV1 activity, we showed that inhibition of PM-resident TRPV1 channels prevented

capsaicin from producing cytosolic Ca^{2+} transients and ER store depletion (**Fig. 5A-D**). Moreover,

activation of PM-resident TRPV1 channels produced Ca^{2+} transients even in the absence of extracellular

Ca^{2+} and also induced ER store depletion (**Fig. 5E-H, fig. S4**). Hence, PM resident TRPV1 channels

must be coupled to ER Ca^{2+} stores through intracellular signaling mechanisms. To probe this, we

demonstrated that TRPV1 activation induced acute PIP_2 hydrolysis, more robustly in the presence of

extracellular Ca^{2+} but also in extracellular Ca^{2+}-free conditions (**fig. S5A, B**). These observations agree

with a previous study (31). The most straightforward mechanism for TRPV1-induced ER store release is

stimulation of Ca^{2+}-dependent PLCδ postulated earlier (31, 59). Some degree of capsaicin-induced ER

store depletion observed in extracellular Ca^{2+}-free conditions is intriguing as it points towards the

existence of additional, hitherto unknown mechanism of coupling, perhaps involving other PLC

isoforms. Identifying this mechanism will require further investigation. Yet, under physiological

conditions, the Ca^{2+}-dependent PLCδ mechanism of IP_3 generation triggered by the Ca^{2+} influx through the TRPV1 channels is likely to be the dominant one.

Our PLA and STORM experiments revealed that a significant fraction of ANO1, TRPV1 and IP_3R channels assemble into complexes containing two of the three, or all three together, with those containing IP_3Rs located at ER-PM junctional nanodomains. At such junctions, B_2Rs, ANO1 (1, 19, 61, 62) and TRPV1 channels (63) are likely anchored within caveolin-1-rich lipid rafts at the PM side of the junction, whereas IP_3Rs at the ER are juxtaposed to ANO1. Using triple-label STORM, we identified the populations of each protein complex containing a combination of ANO1, TRPV1 and IP_3Rs (**Fig. 8, A to C**). Our imaging conditions provided the ability to examine ER-localized IP_3Rs that are proximal to the PM, but we also observed a small percentage of labeled IP_3R1s (11%) that were not co-localized with ANO1 or TRPV1 channels. Based on the proximity analysis of ANO1 and TRPV1 co-localizations, there was a significantly greater likelihood that these channels are also in nanodomain clusters with IP_3R1s, compared to TRPV1-ANO1 clusters without close proximity to IP_3R1. However, not all TRPV1-ANO1 complexes were found being associated with IP_3Rs; this may indicate a separate, direct coupling between TRPV1 and ANO1. Thus, we conclude, based on our functional data, that it is likely that not all ANO1 channels are activated solely through IP_3R-dependent Ca^{2+} signaling (see below). The ANO1-IP_3R1 and TRPV1-IP_3R1 clusters were fewer in quantity overall (which was also consistent with the PLA data), suggesting that physical interaction with IP_3Rs involves both ANO1 and TRPV1 association; this is also supported by the significant reduction in TRPV1-ANO1 coupling after ER Ca^{2+} store depletion. Similar signalling nanodomains may exist in other neuron types, and close association of B_2Rs at the PM and IP_3Rs at the ER membrane has been reported in sympathetic neurons (64, 65). Here we propose that a close-proximity arrangement of ANO1, TRPV1 and IP_3R in DRG neurons ensures that Ca^{2+} influx through TRPV1 provides sufficiently high local $[Ca^{2+}]$ to activate PLCδ, thus ultimately stimulating juxtaposed IP_3Rs that are in direct contact with ANO1 (19, 49); present study; **Fig. 8D**).

As mentioned, our data do not exclude direct coupling between TRPV1 and ANO1, whereby Ca^{2+} influx through the former directly gates the latter (**Fig. 8D**, middle panel). Indeed, some neurons in our assays still produced Ca^{2+}-activated Cl^- currents in response to capsaicin under conditions of ER Ca^{2+} depletion (**fig. S2C** and **Fig. 4B, C**). STORM data suggest that although the majority of multi-channel complexes are composed of all 3 proteins, there is still a sub-population of complexes consisting of only ANO1 and TRPV1, which may mediate such responses independently of IP_3R activation or which may serve as 'specialized' heat sensors, which may only respond to noxious heat. Nevertheless, in the majority of neurons, ER Ca^{2+} release provides at least 50% or more of the Ca^{2+} ions necessary for the full activation of ANO1 by capsaicin-induced TRPV1 activation. This finding and the predominance of ANO1-TRPV1-IP_3R1 complexes over TRPV1-ANO1 complexes (**Fig. 8C**) collectively suggests that IP_3R-mediated Ca^{2+} release is indeed a critical factor for TRPV1-ANO1 coupling in sensory neurons.

One cannot exclude existence of more intricate mechanisms, such as what was previously suggested for the CRAC-ANO1 interplay (58). For instance, Ca^{2+} entering the cytosol through TRPV1 could be taken into the ER by the SERCA pump and then re-released onto the ANO1 channels. The necessity of CRAC to refill the ER stores suggests another intriguing question: whether the association of the multi-channel junctional complex reported here is static or being induced (or modified) in response to G_qPCR activation. Indeed, Orai1 and STIM1 proteins form de novo junctional complexes to assemble into CRAC channels in response to the G_qPCR-induced store depletion (66). Could individual components of ANO1-containing signaling complexes assemble in a similar way upon stimulation? Further research is needed to investigate the dynamics of ANO1-TRPV1-IP_3R1 complex and its possible relationships with CRAC induction mechanisms.

The coupling between the TRPV1 and ANO1 channels in sensory neurons may hold a key to understanding thermal hypersensitivity (hyperalgesia) often produced by local inflammation. Indeed, a functional and/or physical interaction between TRPV1 and ANO1 channels in nociceptors might enable ANO1 to act as an 'amplifier' of TRPV1-mediated excitation, similar to the role of ANO2-mediated

Ca^{2+}-activated Cl^{-} currents in olfactory neurons (67, 68). The contribution of ANO1 activation, which in sensory neurons is excitatory, could then increase the dynamic range of the electrochemical response to noxious heat or inflammation by nociceptors and this coupling may become more important in chronic pain, because the upregulation of both TRPV1 and ANO1 expression in several pain models have been reported (26, 69). It is also important to mention that ANO1 is a downstream component of various inflammatory mediator signaling cascades, which makes it an important player in inflammatory or chronic pain syndromes. The assembly of ANO1 into 'junctional' nanodomains in pain-sensing neurons could also explain how Ca^{2+} signals induced by the relevant stimuli, such as inflammatory mediators or heat, can cause ANO1-mediated excitation, whereas 'irrelevant' Ca^{2+} signals (such as those generated by VGCC during action potential firing) are precluded from having such an effect. Thus, the discovered mechanism exemplifies intricate wiring of intracellular Ca^{2+} signals in neurons providing for a high level of specificity and fidelity of intracellular signaling.

Materials and Methods

Cell culture and transfection

DRGs were extracted from 7 day old Wistar rats and neurons were dissociated as previously described (8, 19). Cultures were maintained on 10 mm glass coverslips pre-coated with poly-D-lysine and laminin and cells were left to grow for 48 hours in DMEM supplemented with GlutaMAX I (Invitrogen), 10% fetal bovine serum, penicillin (50 U/ml), and streptomycin (50 µg/ml) in a humidified incubator (5% CO2, 37°C). For transfection with the EYFP-QL or CEPIA constructs, the Lonza Nucleofector I was used and transfection was done before plating out the cells as described (70).

Live imaging

DRG cultures were loaded with 2 µM fura-2AM (Life Technologies) in the presence of 0.01% pluronic F-127 (Sigma) at 37°C for 45 minutes. Imaging was done using a Nikon TE-2000 microscope (inverted) with a 40x objective and the imaging setup consisted of a Polychrome V monochromator, IMAGO CCD camera and TILLVision 4.5.56 (TillPhotonics) or Live Acquisition 2.2.0 (FEI) software packages. For standard fura-2 imaging (no EYFP-QL transfection), excitation at 340 and 380nm was performed. For fluo-4 imaging, untransfected cells were loaded with fluo-4AM using the same method as for fura-2AM loading. An imaging system comprising of a Nikon TE-2000 E microscope with a DQC-FS camera and a Livescan^{TM} Swept-field confocal system, was utilized for fluo-4 imaging. Analysis was done using Nikon Elements software.

To simultaneously image Ca^{2+} and I^-, DRG neurons (~20 µm diameter) successfully transfected with EYFP-QL and loaded with fura-2 were selected for imaging; glial cells (identified by bipolar processes) were excluded from the analyses. The simultaneous Ca^{2+}/I^- imaging was performed using the UV-2A filter cube (Nikon) and excitation was performed at 340/380 (fura-2) and 488nm (EYFP-QL) wavelengths. Exposure time (typically within 50-200ms for fura-2 and 400-500ms for EYFP-QL) was set for each wavelength on a cell to cell basis, depending on the basal fluorescence intensity. For quadruple wavelength imaging, DRG (transfected with EYFP-QL) loaded with fura-2 were imaged using

340, 380, 488 and 560nm wavelength light using a custom-made dichroic/filter combination DC/59022bs-XR-360-UF1 and DC/59022m; Chroma).

Standard extracellular bath solution consisted of (mM): NaCl (160); KCl (2.5); MgCl$_2$ (1); CaCl$_2$ (2); HEPES (10) and Glucose (10); pH adjusted to 7.4 with NaOH (All from Sigma). I$^-$ containing solutions were produced by equimolar substitution of the NaCl with NaI (30 mM, 10 mM or 5mM). Compounds were added to the NaI containing solution whilst imaging: GABA, 100 μM (Tocris); capsaicin, 1 μM (Sigma); bradykinin, 250 nM (Merck), ruthenium red, 10 μM (Sigma). K2 was a generous gift from Dr. Avi Priel (The Institute for Drug Research, School of Pharmacy, Faculty of Medicine, The Hebrew University of Jerusalem). The depolarizing 50 mM K$^+$ solution was produced by equimolar substitution of NaCl with KCl. Ca^{2+}-free solutions were produced with increased NaCl (165 mM) to compensate for Cl$^-$ lost with the removal of CaCl$_2$; 1 mM EGTA was also added. Pre-incubation with thapsigargin (1 μM; LKT Laboratories) or cyclopiazonic acid (1 μM; Tocris) was done during the fura-2 loading process where required and the compound was also kept in solutions throughout imaging. Gravity bath perfusion was used for all experiments apart from those involving K2, for which an Automate Scientific SmartSquirt Microperfusion system was utilized. A fine 100μm tip was used with this system and pressure was maintained at 3psi for all experiments using this perfusion method. The tip was positioned over DRG neurons selected for testing under 10x or 40x magnification before being activated.

Imaging data analysis

Analysis of primary data and statistics were performed in Microsoft Excel, Origin Pro and GraphPad Prism 8. Fura-2 ratios were normalized to R value at t=0 (R_0) and expressed as a difference from R/R_0 ($\Delta R/R_0$). EYFP-QL fluorescence intensity was normalized to fluorescence at t=0 (F_0) and expressed as a difference from F_0 ($\Delta F/F_0$), for each cell. Data from all cells were temporarily aligned to the point of R/R_0 increase by 3 times the standard deviation of the baseline. Agonist-dependent EYFP-QL

fluorescence quenching or red-CEPIA fluorescence intensity change were quantified from this point until the end of agonist application. Where possible, linear agonist-independent run-down of fluorescence signals was corrected before final analysis.

Electrophysiology

Whole cell voltage clamp recordings were performed as previously described (8). Patch electrodes were pulled from borosilicate glass and fire polished to a final resistance of 2–4 MΩ. An EPC-10 patch clamp amplifier in combination with Patchmaster version 2x35 software (HEKA) was used. Standard extracellular bath solution consisted of (mM): NaCl (160); KCl (2.5); $MgCl_2$ (1); $CaCl_2$ (2); HEPES (10) and glucose (10); pH adjusted to 7.4 with NaOH (all from Sigma). The internal pipette solution consisted of (mM): CsCl (150); $MgCl_2$ (5); K_2ATP (1); NaGTP (0.1); EGTA (1) and HEPES (10). pH adjusted to 7.4 with CsOH (all from Sigma). After obtaining a gigaseal, whole cell configuration was attained and gap-free recordings performed at a holding voltage of -60mV. Capsaicin (1 µM) was applied to DRG neurons with or without 30 min pre-incubation with Ani9 (500 nM; Tocris) or thapsigargin (1 µM). Fitmaster v2x73.5 (HEKA) has been used for data analysis.

PLCδ-PH-GFP translocation

Cultured DRG neurons were transfected with the PLCδ-PH-GFP construct using the same method as for EYFP-QL and CEPIA transfection (see above). The Nikon confocal imaging and analysis system used for fluo-4AM live Ca^{2+} imaging was also used for PLCδ-PH-GFP translocation assays. GFP fluorescence intensity in the cytosolic regions of the cell was used as a measure of the probe translocation.

Proximity Ligation Assay (PLA)

PLA was performed using PLA kits (Sigma) as previously described (19). Antibodies used were ANO1 (1:200; Santa Cruz or 1:500; Abcam), TRPV1 (1:500; Neuromics) and IP_3R1 (1:500; Calbiochem), CD71 (1:500, Santa Cruz). For anti-guinea pig antibodies (such as TRPV1), PLA 'minus' probes were manually conjugated onto an anti-guinea pig IgG antibody using a PLA conjugation kit. DRG cultures were prepared and plated on microscope slides (coated with poly-d-lysine and laminin)

and permeabilized using acetone:methanol (1:1) on ice for 20 minutes and washed with PBS 3 times. Hydrophobic barriers were made on the slides using an ImmEdge hydrophobic barrier pen (Vector laboratories) to delimit reactions to ~1cm^2 and blocking was done using the PLA blocking reagent for 30 minutes in a humidified incubator (37°C). Primary antibodies were then applied and left at 4°C overnight. The following day, PLA probes were applied to the samples; signals were amplified and detected according to the manufacturer's instructions; and slides were sealed with DAPI-containing mounting medium (Sigma). Samples were imaged using the Zeiss LSM700 confocal microscope. Green fluorescent puncta (0.5-1µm) were counted per cell using Zen imaging software (Zeiss).

Statistical analysis

Data are presented as mean ± S.E.M unless stated. Data were tested for normality and either parametric (Student's t-test, ANOVA) or non-parametric (Wilcoxon signed-rank test; Mann Whitney test, Kruskal-Wallis ANOVA) tests were carried out. Difference between means was considered significant at $p < 0.05$. Approach to analysis of STORM data is described below.

Stochastic Optical Reconstruction Microscopy (STORM)

All images were acquired on a Nikon N-STORM super-resolution system (Nikon Instruments Inc.), consisting of a Nikon Eclipse Ti inverted microscope and an astigmatic 3D lens placed in front of the EMCCD camera to allow the Z coordinates to be most accurately determined. The laser set-up of our STORM system allows for the multiple, largely non-overlapping activator dyes, Alexa Fluor 405 carboxylic acid (Invitrogen, #A30000), Cy2 bisreactive dye pack (GE Healthcare, #PA22000), and Cy3 mono-reactive dye pack (GE Healthcare, #PA23001), to be conjugated to affinity-purified secondary antibodies from Jackson Immunoresearch, along with the reporter dye, Alexa Fluor 647 carboxylic acid (Invitrogen, #A20006) in order to acquire images from three different protein labels in the same experiment. Using the same primary antibodies used in the PLA experiments, we determined the extent of co-localization of TRPV1, ANO1, and IP$_3$R1, as individual multi-protein complexes with either two or three photo-switchable dye activators, Alexa Fluor 405, Cy2, and Cy3, coupled to three distinct

secondary antibodies (raised in different species) labeling the proteins in DRGs. The activator and reporter fluorophores were conjugated in-house to an appropriate unlabeled secondary antibody (71). STORM imaging was performed in a freshly prepared imaging buffer that contained (in mM): 50 Tris (pH 8.0), 10 NaCl and 10% (w/v) glucose, with an oxygen-scavenging GLOX solution (0.5mg/ml glucose oxidase (Sigma-Aldrich), 40 μg/ml catalase (Sigma-Aldrich), and 10 mM cysteamine MEA (Sigma-Aldrich). MEA was prepared fresh as a 1 M stock solution in water, stored at 4°C and used within 1 month of preparation. Acquisitions were made from between 2-4 different experiments for labeling and imaging. Images were rendered as a 2D Gaussian fit of each localization. The diameter of each point is representative of the localization precision (larger diameter, less precise), as is intensity (more intense, more precise). Signal-noise thresholds were handled as peak height above the local background in the N-STORM software (Elements). A detected peak was set as the central pixel in a 5x5 pixel area, and the average intensity of the 4 corner pixels was subtracted from intensity of the central pixel. Using a 100x objective and 16x16μm pixel area of the iXon3 camera, this corresponds to a 0.8x0.8μm physical neighborhood.

Adjustment of STORM localizations for differential rates of dye bleaching

The STORM acquisitions were carried out for a minimum of 6,000 activator-reporter cycles and until at least one of three activator laser wavelengths no longer registered localizations. We observed that the Alexa Fluor 405-Alexa Fluor 647 dye pair persisted stably for more cycles than the Cy2-Alexa Fluor 647 or Cy3-Alexa Fluor 647 dye pairs, independent of the secondary antibody that was conjugated (**fig. S8**). Therefore, we concluded that the Cy2 and Cy3 dyes bleach out more rapidly than Alexa Fluor 405 after many repeated activation cycles. Such differential rates of photobleaching would cause us to over-estimate the number of complexes containing a protein labeled by Alexa Fluor 405, and possibly under-estimate those without. Hence, we corrected for this artifact to the best of our ability. To more adequately compare the STORM localizations in the triple-labeled conditions, we first determined a linear approximation of the differential exponential decay of localizations for each corresponding activator dye.

The cumulative probability distributions demonstrated that Alexa Fluor 405 had a significantly greater number of localizations than equally labeled Cy2 or Cy3 at approximately 3,000 laser activation cycles (36,000 total frames) and beyond **(fig. S8)**. The factor of decay was used to time-dependently correct for this by probabilistically excluding Alexa Fluor 405-specific localizations from the cluster detection analysis to compensate for this, preventing oversampling above that of Cy2 or Cy3 molecules. After this adjustment, the numbers of clusters of each combination of multi-channel complexes did not significantly change due to the details of our sampling paradigm, except for those of Alexa Fluor 405-only centroid clusters. We estimate that the applied compensation paradigm corrected for the above mentioned artifact by >90%.

Cluster size and localization proximity analysis

Unfiltered STORM localization data were exported as molecular list text files from Nikon-Elements and were analyzed with in-house software incorporating a density-based spatial clustering of applications with noise (DBSCAN) (72). A dense region or cluster was defined as localizations within a directly-reachable radius proximity (epsilon) from a criterion minimum number of other core localizations (MinPts). Density-reachable points were localizations that were within the epsilon radius of a single core point and thus considered part of the cluster. Localizations considered to be noise were points that were not within the epsilon distance of any core points of a cluster. We derived the appropriate epsilon parameter using the nearest-neighbor plot from single-dye labeled controls; cluster detection was determined for epsilon between 20 and 80nm, which were the nearest-neighbor localization distances representing 95% of area under the curve. DBSCAN parameters were verified by measuring goodness of fit to Gaussian distribution with cluster population data from single-dye labeled controls, and set for distance of directly reachable points at 50nm (epsilon) and 7 minimum points (MinPts). These parameters were found to be the most stringent possible, that also reliably fit the control data. For cluster detection, each localization was assessed based on its corrected X and corrected Y 2D spatial coordinates, and the associated activator dye was tracked throughout analysis. Detected clusters were tabulated by the

composition of resident activator dyes contributing to the total neighborhood of localizations for that cluster. Clusters were categorized based on activator dye composition as Alexa Fluor 405 only, Cy2 only, Cy3 only, Alexa Fluor 405 + Cy2, Alexa Fluor 405 + Cy3, or Alexa Fluor 405 + Cy2 + Cy3, according to the dye conjugated to each antibody label. Cluster radius size (nm) data were placed in probability distribution histograms with bin size of 5nm. Based on the observation that a majority of cluster distributions displayed positive skew, distributions were fit by the generalized extreme value distribution function: $f(x) = e^{-(x-1+e^{-x})}$. Cluster size values were reported as mean ± SEM. The β continuous scale parameter of each cluster distribution was derived from the mean value of the extreme distribution (Mean $= \mu + \gamma\beta$, γ: 0.5772, Euler-Mascheroni constant) and was determined as a metric for "tailedness" of cluster size distribution. In addition, the percentage of clusters belonging to a labeling category out of total clusters was compared. Cumulative distribution functions of cluster categories were compared with the Kolmogorov-Smirnov test. Population statistics for each cluster category were derived from 6-12 cells per staining and imaging condition.

Supplementary Materials

Fig. S1 Depolarization-induced I⁻ influx is a Ca²⁺-independent phenomenon

Fig. S2 ER Ca²⁺ store depletion severely reduces Ca²⁺ transients and CaCC activation in response to capsaicin

Fig. S3 Capsaicin applied in extracellular Ca²⁺-free conditions and acute thapsigargin-induced ER Ca²⁺ leak can induce a degree of CaCC activation

Fig. S4 The cell-impermeable TRPV1 agonist K2 evokes cytosolic Ca²⁺ transients in the absence of extracellular Ca²⁺

Fig. S5 Capsaicin induces PLC activation in DRG neurons

Fig. S6 Controls for PLA

Fig. S7 CD71 and IP$_3$R1 are not found in close proximity as confirmed by PLA and STORM analysis

Fig. S8 Decay rates of STORM fluorescent dye labels after repeated laser activation cycles

Table S1. Mean percentages of STORM cluster distributions detected by DBSCAN

Table S2. Mean cluster radius sizes of STORM-derived clusters detected by DBSCAN

Table S3. Mean number of localizations per cluster from STORM-derived clusters detected by DBSCAN

References and Notes

1. X. Jin, S. Shah, X. Du, H. Zhang, N. Gamper, Activation of Ca^{2+}-activated Cl^- channel ANO1 by localized Ca^{2+} signals. J Physiol **594**, 19-30 (2016).
2. C. Hartzell, I. Putzier, J. Arreola, Calcium-activated chloride channels. Annu Rev Physiol **67**, 719-758 (2005).
3. N. Pedemonte, L. J. Galietta, Structure and function of TMEM16 proteins (anoctamins). Physiol Rev **94**, 419-459 (2014).
4. F. Huang, X. Wong, L. Y. Jan, International Union of Basic and Clinical Pharmacology. LXXXV: calcium-activated chloride channels. Pharmacol Rev **64**, 1-15 (2012).
5. A. Caputo, E. Caci, L. Ferrera, N. Pedemonte, C. Barsanti, E. Sondo, U. Pfeffer, R. Ravazzolo, O. Zegarra-Moran, L. J. Galietta, TMEM16A, a membrane protein associated with calcium-dependent chloride channel activity. Science **322**, 590-594 (2008).
6. B. C. Schroeder, T. Cheng, Y. N. Jan, L. Y. Jan, Expression cloning of TMEM16A as a calcium-activated chloride channel subunit. Cell **134**, 1019-1029 (2008).
7. Y. D. Yang, H. Cho, J. Y. Koo, M. H. Tak, Y. Cho, W. S. Shim, S. P. Park, J. Lee, B. Lee, B. M. Kim, R. Raouf, Y. K. Shin, U. Oh, TMEM16A confers receptor-activated calcium-dependent chloride conductance. Nature **455**, 1210-1215 (2008).
8. B. Liu, J. E. Linley, X. Du, X. Zhang, L. Ooi, H. Zhang, N. Gamper, The acute nociceptive signals induced by bradykinin in rat sensory neurons are mediated by inhibition of M-type K^+ channels and activation of Ca^{2+}-activated Cl^- channels. J Clin Invest **120**, 1240-1252 (2010).
9. H. Cho, Y. D. Yang, J. Lee, B. Lee, T. Kim, Y. Jang, S. K. Back, H. S. Na, B. D. Harfe, F. Wang, R. Raouf, J. N. Wood, U. Oh, The calcium-activated chloride channel anoctamin 1 acts as a heat sensor in nociceptive neurons. Nat Neurosci **15**, 1015-1021 (2012).
10. Y. Takayama, D. Uta, H. Furue, M. Tominaga, Pain-enhancing mechanism through interaction between TRPV1 and anoctamin 1 in sensory neurons. Proc Natl Acad Sci U S A **112**, 5213-5218 (2015).
11. K. Funk, A. Woitecki, C. Franjic-Wurtz, T. Gensch, F. Mohrlen, S. Frings, Modulation of chloride homeostasis by inflammatory mediators in dorsal root ganglion neurons. Mol Pain **4**, 32 (2008).
12. S. Pieraut, V. Laurent-Matha, C. Sar, T. Hubert, I. Mechaly, C. Hilaire, M. Mersel, E. Delpire, J. Valmier, F. Scamps, NKCC1 phosphorylation stimulates neurite growth of injured adult sensory neurons. J Neurosci **27**, 6751-6759 (2007).
13. Q. Xiao, K. Yu, P. Perez-Cornejo, Y. Cui, J. Arreola, H. C. Hartzell, Voltage- and calcium-dependent gating of TMEM16A/Ano1 chloride channels are physically coupled by the first intracellular loop. Proc Natl Acad Sci U S A **108**, 8891-8896 (2011).
14. C. Paulino, V. Kalienkova, A. K. M. Lam, Y. Neldner, R. Dutzler, Activation mechanism of the calcium-activated chloride channel TMEM16A revealed by cryo-EM. Nature **552**, 421-425 (2017).
15. J. A. Contreras-Vite, S. Cruz-Rangel, J. J. De Jesus-Perez, I. A. Figueroa, A. A. Rodriguez-Menchaca, P. Perez-Cornejo, H. C. Hartzell, J. Arreola, Revealing the activation pathway for TMEM16A chloride channels from macroscopic currents and kinetic models. Pflugers Arch **468**, 1241-1257 (2016).
16. X. Du, H. Hao, S. Gigout, D. Huang, Y. Yang, L. Li, C. Wang, D. Sundt, D. B. Jaffe, H. Zhang, N. Gamper, Control of somatic membrane potential in nociceptive neurons and its implications for peripheral nociceptive transmission. Pain **155**, 2306-2322 (2014).
17. D. Sapunar, M. Ljubkovic, P. Lirk, J. B. McCallum, Q. H. Hogan, Distinct membrane effects of spinal nerve ligation on injured and adjacent dorsal root ganglion neurons in rats. Anesthesiology **103**, 360-376 (2005).

18. R. Amir, C. N. Liu, J. D. Kocsis, M. Devor, Oscillatory mechanism in primary sensory neurones. Brain **125**, 421-435 (2002).
19. X. Jin, S. Shah, Y. Liu, H. Zhang, M. Lees, Z. Fu, J. D. Lippiat, D. J. Beech, A. Sivaprasadarao, S. A. Baldwin, H. Zhang, N. Gamper, Activation of the Cl$^-$ Channel ANO1 by Localized Calcium Signals in Nociceptive Sensory Neurons Requires Coupling with the IP$_3$ Receptor. Sci Signal **6**, ra73 (2013).
20. S. M. Ward, J. L. Kenyon, The spatial relationship between Ca^{2+} channels and Ca^{2+}-activated channels and the function of Ca^{2+}-buffering in avian sensory neurons. Cell Calcium **28**, 233-246 (2000).
21. R. Bao, L. M. Lifshitz, R. A. Tuft, K. Bellve, K. E. Fogarty, R. ZhuGe, A close association of RyRs with highly dense clusters of Ca^{2+}-activated Cl$^-$ channels underlies the activation of STICs by Ca2+ sparks in mouse airway smooth muscle. J Gen Physiol **132**, 145-160 (2008).
22. P. J. Bauer, The local Ca concentration profile in the vicinity of a Ca channel. Cell Biochem Biophys **35**, 49-61 (2001).
23. R. Rizzuto, T. Pozzan, Microdomains of intracellular Ca^{2+}: molecular determinants and functional consequences. Physiol Rev **86**, 369-408 (2006).
24. J. E. Linley, K. Rose, L. Ooi, N. Gamper, Understanding inflammatory pain: ion channels contributing to acute and chronic nociception. Pflugers Arch **459**, 657-669 (2010).
25. G. Petho, P. W. Reeh, Sensory and signaling mechanisms of bradykinin, eicosanoids, platelet-activating factor, and nitric oxide in peripheral nociceptors. Physiol Rev **92**, 1699-1775 (2012).
26. B. Lee, H. Cho, J. Jung, Y. D. Yang, D. J. Yang, U. Oh, Anoctamin 1 contributes to inflammatory and nerve-injury induced hypersensitivity. Mol Pain **10**, 5 (2014).
27. F. Ru, H. Sun, D. Jurcakova, R. A. Herbstsomer, J. Meixong, X. Dong, B. J. Undem, Mechanisms of pruritogen-induced activation of itch nerves in isolated mouse skin. J Physiol, (2017).
28. K. Kunzelmann, I. Cabrita, P. Wanitchakool, J. Ousingsawat, L. Sirianant, R. Benedetto, R. Schreiber, Modulating Ca^{2+} signals: a common theme for TMEM16, Ist2, and TMC. Pflugers Arch **468**, 475-490 (2016).
29. Y. Dai, T. Moriyama, T. Higashi, K. Togashi, K. Kobayashi, H. Yamanaka, M. Tominaga, K. Noguchi, Proteinase-activated receptor 2-mediated potentiation of transient receptor potential vanilloid subfamily 1 activity reveals a mechanism for proteinase-induced inflammatory pain. J Neurosci **24**, 4293-4299 (2004).
30. D. S. Samways, B. S. Khakh, T. M. Egan, Tunable calcium current through TRPV1 receptor channels. J Biol Chem **283**, 31274-31278 (2008).
31. V. Lukacs, Y. Yudin, G. R. Hammond, E. Sharma, K. Fukami, T. Rohacs, Distinctive changes in plasma membrane phosphoinositides underlie differential regulation of TRPV1 in nociceptive neurons. J Neurosci **33**, 11451-11463 (2013).
32. L. J. Galietta, P. M. Haggie, A. S. Verkman, Green fluorescent protein-based halide indicators with improved chloride and iodide affinities. FEBS Lett **499**, 220-224 (2001).
33. T. Johansson, T. Norris, H. Peilot-Sjogren, Yellow fluorescent protein-based assay to measure GABA(A) channel activation and allosteric modulation in CHO-K1 cells. PLoS One **8**, e59429 (2013).
34. W. Namkung, Z. Yao, W. E. Finkbeiner, A. S. Verkman, Small-molecule activators of TMEM16A, a calcium-activated chloride channel, stimulate epithelial chloride secretion and intestinal contraction. FASEB J **25**, 4048-4062 (2011).
35. X. Du, H. Hao, Y. Yang, S. Huang, C. Wang, S. Gigout, R. Ramli, X. Li, E. Jaworska, I. Edwards, J. Deuchars, Y. Yanagawa, J. Qi, B. Guan, D. B. Jaffe, H. Zhang, N. Gamper, Local GABAergic signaling within sensory ganglia controls peripheral nociceptive transmission. J Clin Invest **127**, 1741-1756 (2017).

36.	B. Robertson, Characteristics of GABA-activated chloride channels in mammalian dorsal root ganglion neurones. J Physiol **411**, 285-300 (1989).
37.	J. P. Gallagher, H. Higashi, S. Nishi, Characterization and ionic basis of GABA-induced depolarizations recorded in vitro from cat primary afferent neurones. J Physiol **275**, 263-282 (1978).
38.	Y. Seo, H. K. Lee, J. Park, D. K. Jeon, S. Jo, M. Jo, W. Namkung, Ani9, A Novel Potent Small-Molecule ANO1 Inhibitor with Negligible Effect on ANO2. PLoS One **11**, e0155771 (2016).
39.	L. S. Premkumar, G. P. Ahern, Induction of vanilloid receptor channel activity by protein kinase C. Nature **408**, 985-990 (2000).
40.	J. Suzuki, K. Kanemaru, K. Ishii, M. Ohkura, Y. Okubo, M. Iino, Imaging intraorganellar Ca^{2+} at subcellular resolution using CEPIA. Nat Commun **5**, 4153 (2014).
41.	V. Lukacs, B. Thyagarajan, P. Varnai, A. Balla, T. Balla, T. Rohacs, Dual regulation of TRPV1 by phosphoinositides. J Neurosci **27**, 7070-7080 (2007).
42.	K. C. Thomas, A. S. Sabnis, M. E. Johansen, D. L. Lanza, P. J. Moos, G. S. Yost, C. A. Reilly, Transient receptor potential vanilloid 1 agonists cause endoplasmic reticulum stress and cell death in human lung cells. J Pharmacol Exp Ther **321**, 830-838 (2007).
43.	C. J. Bohlen, A. Priel, S. Zhou, D. King, J. Siemens, D. Julius, A bivalent tarantula toxin activates the capsaicin receptor, TRPV1, by targeting the outer pore domain. Cell **141**, 834-845 (2010).
44.	E. Cao, M. Liao, Y. Cheng, D. Julius, TRPV1 structures in distinct conformations reveal activation mechanisms. Nature **504**, 113-118 (2013).
45.	C. Bae, C. Anselmi, J. Kalia, A. Jara-Oseguera, C. D. Schwieters, D. Krepkiy, C. Won Lee, E. H. Kim, J. I. Kim, J. D. Faraldo-Gomez, K. J. Swartz, Structural insights into the mechanism of activation of the TRPV1 channel by a membrane-bound tarantula toxin. eLife **5**, (2016).
46.	M. Geron, R. Kumar, W. Zhou, J. D. Faraldo-Gomez, V. Vasquez, A. Priel, TRPV1 pore turret dictates distinct DkTx and capsaicin gating. Proc Natl Acad Sci U S A **115**, E11837-E11846 (2018).
47.	N. Gamper, T. Rohacs, Phosphoinositide sensitivity of ion channels, a functional perspective. Subcell Biochem **59**, 289-333 (2012).
48.	E. J. Dickson, B. Hille, Understanding phosphoinositides: rare, dynamic, and essential membrane phospholipids. Biochem J **476**, 1-23 (2019).
49.	I. Cabrita, R. Benedetto, A. Fonseca, P. Wanitchakool, L. Sirianant, B. V. Skryabin, L. K. Schenk, H. Pavenstadt, R. Schreiber, K. Kunzelmann, Differential effects of anoctamins on intracellular calcium signals. FASEB J **31**, 2123-2134 (2017).
50.	I. Weibrecht, K. J. Leuchowius, C. M. Clausson, T. Conze, M. Jarvius, W. M. Howell, M. Kamali-Moghaddam, O. Soderberg, Proximity ligation assays: a recent addition to the proteomics toolbox. Expert Rev Proteomics **7**, 401-409 (2010).
51.	O. Soderberg, M. Gullberg, M. Jarvius, K. Ridderstrale, K. J. Leuchowius, J. Jarvius, K. Wester, P. Hydbring, F. Bahram, L. G. Larsson, U. Landegren, Direct observation of individual endogenous protein complexes in situ by proximity ligation. Nat Methods **3**, 995-1000 (2006).
52.	J. Zhang, C. M. Carver, F. S. Choveau, M. S. Shapiro, Clustering and Functional Coupling of Diverse Ion Channels and Signaling Proteins Revealed by Super-resolution STORM Microscopy in Neurons. Neuron **92**, 461-478 (2016).
53.	M. Amsalem, Poilbout, C., Ferracci, G., Delmas, P., Padilla, F., Membrane cholesterol depletion as a trigger of Nav1.9 channel-mediated inflammatory pain. EMBO J **37**, pii: e97349 (2018).
54.	A. Dani, B. Huang, J. Bergan, C. Dulac, X. Zhuang, Superresolution imaging of chemical synapses in the brain. Neuron **68**, 843-856 (2010).

55. M. J. Rust, M. Bates, X. Zhuang, Sub-diffraction-limit imaging by stochastic optical reconstruction microscopy (STORM). Nat Methods **3**, 793-795 (2006).
56. D. Axelrod, Total internal reflection fluorescence microscopy in cell biology. Methods Enzymol **361**, 1-33 (2003).
57. M. Bal, O. Zaika, P. Martin, M. S. Shapiro, Calmodulin binding to M-type K^+ channels assayed by TIRF/FRET in living cells. J Physiol **586**, 2307-2320 (2008).
58. R. Courjaret, K. Machaca, Mid-range Ca^{2+} signalling mediated by functional coupling between store-operated Ca^{2+} entry and IP_3-dependent Ca^{2+} release. Nat Commun **5**, 3916 (2014).
59. T. Rohacs, Phosphoinositide signaling in somatosensory neurons. Adv Biol Regul **61**, 2-16 (2016).
60. S. Gallego-Sandin, A. Rodriguez-Garcia, M. T. Alonso, J. Garcia-Sancho, The endoplasmic reticulum of dorsal root ganglion neurons contains functional TRPV1 channels. J Biol Chem **284**, 32591-32601 (2009).
61. N. A. Jeske, Somatosensory scaffolding structures. Front Mol Neurosci **5**, 2 (2012).
62. N. A. Jeske, K. A. Berg, J. C. Cousins, E. S. Ferro, W. P. Clarke, M. J. Glucksman, J. L. Roberts, Modulation of bradykinin signaling by EP24.15 and EP24.16 in cultured trigeminal ganglia. J Neurochem **97**, 13-21 (2006).
63. E. Szoke, R. Borzsei, D. M. Toth, O. Lengl, Z. Helyes, Z. Sandor, J. Szolcsanyi, Effect of lipid raft disruption on TRPV1 receptor activation of trigeminal sensory neurons and transfected cell line. Eur J Pharmacol **628**, 67-74 (2010).
64. P. Delmas, N. Wanaverbecq, F. C. Abogadie, M. Mistry, D. A. Brown, Signaling microdomains define the specificity of receptor-mediated $InsP_3$ pathways in neurons. Neuron **34**, 209-220. (2002).
65. N. Gamper, V. Reznikov, Y. Yamada, J. Yang, M. S. Shapiro, Phosphatidylinositol 4,5-bisphosphate signals underlie receptor-specific $G_{q/11}$-mediated modulation of N-type Ca^{2+} channels. J Neurosci **24**, 10980-10992 (2004).
66. M. D. Cahalan, STIMulating store-operated Ca^{2+} entry. Nat Cell Biol **11**, 669-677 (2009).
67. S. Pifferi, V. Cenedese, A. Menini, Anoctamin 2/TMEM16B: a calcium-activated chloride channel in olfactory transduction. Exp Physiol **97**, 193-199 (2012).
68. A. B. Stephan, E. Y. Shum, S. Hirsh, K. D. Cygnar, J. Reisert, H. Zhao, ANO2 is the cilial calcium-activated chloride channel that may mediate olfactory amplification. Proc Natl Acad Sci U S A **106**, 11776-11781 (2009).
69. Y. Kanai, E. Nakazato, A. Fujiuchi, T. Hara, A. Imai, Involvement of an increased spinal TRPV1 sensitization through its up-regulation in mechanical allodynia of CCI rats. Neuropharmacology **49**, 977-984 (2005).
70. H. M. Kirton, L. Pettinger, N. Gamper, Transient overexpression of genes in neurons using nucleofection. Methods Mol Biol **998**, 55-64 (2013).
71. G. T. Dempsey, J. C. Vaughan, K. H. Chen, M. Bates, X. Zhuang, Evaluation of fluorophores for optimal performance in localization-based super-resolution imaging. Nat Methods **8**, 1027-1036 (2011).
72. Ester M, Kriegel HP, Sander H, Xu X (1996) A Density-Based Algorithm for Discovering Clusters in Large Spatial Datasets with Noise. In Proc 2nd Int Conf KDDD, pp 1232-1239. Portland, Oregon.

Figure legends

Figure 1. Optical interrogation of Cl⁻ channel activity in DRG neurons. (A) Schematic of the dual imaging protocol. DRG neurons are transfected with EYFP (H148Q/I152L); NaI (I⁻) is added to the extracellular solutions. Upon stimulation of GPCRs such as the bradykinin receptor B_2R, Ca^{2+} is released from the endoplasmic reticulum (ER) through the IP_3R. This rise in intracellular Ca^{2+} is detected by fura-2 (depicted as brightening of cytosol in the middle and right panels). Activation of ANO1 channels by released Ca^{2+} results in I⁻ influx, which, in turn induces quenching of the EYFP-QL fluorescence (right panel). **(B)** Schematic of expected EYFP (H148Q/I152L) quenching in response to ANO1-mediated I⁻ influx (30 mM extracellular NaI; based on (19)). **(C)** Schematic of the optimized protocol developed in this study. The concentration of NaI is reduced in steps to develop a protocol with minimal agonist-independent quenching and sufficient dynamic range. **(D)** Representative traces of EYFP (H148Q/I152L) fluorescence quenching produced by 5 mM (black trace), 10 mM (red trace) and 30 mM (grey trace) extracellular NaI and subsequently added GABA (100 µM). **(E)** Scatter plots summarizing experiments similar to those shown in (D); 5 mM: n=5 neurons, 10 mM: n=5 neurons and 30 mM: n=7 neurons. Quenching produced after standard bath solution application (black circle), NaI application (red triangle) and NaI and GABA (100 µM) application (grey triangles). Asterisks denote the following: *p<0.05 and ***p<0.001 (paired t-test); n.s, not significant.

Figure 2. All-optical demonstration of coupling of CaCC activation to IP_3R-mediated Ca^{2+} release. (A, B) Representative traces showing Ca^{2+} rises and concurrent EYFP-QL fluorescence quenching in small-diameter DRG neurons transfected with EYFP-QL and loaded with fura-2AM in response to BK (250 nM) application in the absence (A) or presence (B) of ANO1 inhibitors, T16A-inhA01 (50 µM) or Ani9 (500 nM). **(C)** Scatter plots summarizing experiments similar to those shown in (A); BK: n=12 neurons, (B); T16A-inhA01: n=6 neurons and Ani9: n=7 neurons. **(D)** Representative

trace showing fura-2 and EYFP-QL responses to BK application in DRG neurons when Ca^{2+} was omitted from the extracellular solutions. **(E)** Comparison between the data for BK application with (n=12 neurons) and without extracellular Ca^{2+} (n=5 neurons). In C and E, asterisks denote the following: *p<0.05, **p<0.01 and ***p<0.001; n.s, not significant (paired or unpaired t-test, as appropriate).

Figure 3. ER Ca^{2+} release is required for the TRPV1-mediated activation of CaCC. (A) Representative trace showing a Ca^{2+} rise and a concurrent EYFP-QL fluorescence quenching in a small-diameter DRG neuron transfected with EYFP-QL and loaded with fura-2AM in response to capsaicin (1 μM) application. **(B)** Scatter plots summarizing experiments similar to those shown in (A); n=9 neurons. **(C)** Comparisons for the fura-2 ratiometric Ca^{2+} measurement and EYFP-QL fluorescence quenching in response to capsaicin and BK application. **(D)** Summary of fura-2 Ca^{2+} imaging experiments in which capsaicin was applied either under control conditions (n=19 neurons), in the presence of thapsigargin (TG; 1μM; n=12 neurons), with no extracellular Ca^{2+} (n=9 neurons), or in the presence of cyclopiazonic acid (CPA; 1μM; n=16 neurons). **(E)** Representative traces showing a response to capsaicin in triple imaging experiments, where fura-2 Ca^{2+} levels (black trace), EYFP-QL fluorescence quenching (red trace) and ER-Ca^{2+} levels using red-CEPIA (grey trace) were simultaneously monitored in EYFP-QL and red-CEPIA co-transfected DRG neurons. **(F)** Scatter plots summarizing experiments similar to those shown in (E), n=8 neurons. In B-F, asterisks denote the following: *p<0.05, **p<0.01 and ***p<0.001; n.s, not significant (B, F: paired t-test and Wilcoxon signed-rank test; C: unpaired t-test; D: one-way ANOVA).

Figure 4. Thapsigargin disrupts capsaicin-induced currents in small-diameter DRG neurons. **(A)** Representative whole-cell patch clamp recordings from DRG neurons held at -60mV during application of capsaicin (1 μM) in the absence (black trace) or presence (red trace) of the ANO1 inhibitor Ani9 (500 nM). **(B)** Responses to capsaicin (1 μM) in the presence of thapsigargin (TG; 1 μM).

Capsaicin-induced currents that were smaller (black trace) or of comparable amplitude (red trace) to those obtained under control conditions are shown. (**C**) Scatter plots summarizing areas under the curve for capsaicin responses in experiments similar to these shown in (A, B); control (n=18 neurons), Ani9 (n=11 neurons); TG (n=16 neurons). In C, asterisks denote the following: *p<0.05; n.s, not significant (Kruskal-Wallis ANOVA with Mann-Whitney test).

Figure 5. ER-localized TRPV1 channels are not engaged during extracellular TRPV1 stimulation in small-diameter DRG neurons. (A) Representative traces showing Ca^{2+} responses in small-diameter DRG neurons loaded with fluo-4AM in response to capsaicin (1 μM) in the presence of ruthenium red (RR; 10 μM) and after the RR washout. **(B)** Scatter plots summarizing experiments similar to those shown in (A); RR + CAP (n=42 neurons); CAP (n=38 neurons). **(C)** Representative trace showing fluorescence changes in a small-diameter DRG neurons transfected with green-CEPIA in response to capsaicin (1 μM) in the presence of RR (10 μM) and after the RR washout. **(D)** Scatter plots summarizing experiments similar to those shown in (C); n=6 neurons. **(E)** Representative traces showing a Ca^{2+} response in a small-diameter DRG neuron loaded with fura-2AM in response to capsaicin (1 μM) and K2 (30 μM). **(F)** Scatter plots summarizing experiments similar to those shown in (E); CAP n=19 neurons; K2 n=19 neurons; K2 (Ca^{2+} free) n=8 neurons. **(G)** Representative trace showing fluorescence changes in a small-diameter DRG neuron transfected with red-CEPIA in response to K2 (30 μM). **(H)** Scatter plots summarizing experiments similar to those shown in (F); K2 CEPIA n=8 neurons; NR K2 CEPIA n=4 neurons. In B, D, F, asterisks denote the following: *p<0.05, **p<0.01 and ***p<0.001; n.s, not significant (B: Mann-Whitney test; D: paired t-test; F: Kruskal-Wallis ANOVA with Mann-Whitney test; H: unpaired t-test).

Figure 6. ANO1, TRPV1 and IP$_3$R1s are in close proximity in small-diameter DRG neurons as tested with Proximity Ligation Assay (PLA). (A-C) PLA images for TRPV1-ANO1 (A), ANO1-IP$_3$R1 (B) and TRPV1-IP$_3$R1 (C) pairs in DRG cultures. Left panels: brightfield images; middle panels: PLA puncta detection; right panels: merged images of brightfield and PLA puncta. Scale bars represent 20 μm. **(D)** Scatter plots summarizing number of PLA puncta per cell in experiments similar to these shown in (A-C); TRPV1-ANO1 (n=41 neurons), ANO1-IP$_3$R1 (n=16 neurons); TRPV1-IP$_3$R1 (n=16 neurons); black outlined symbols depict negative control where only one primary antibody (against ANO1) was used in conjunction with both PLA secondary probes (**fig. S6A, B**). In D, asterisks denote the following: ***$p < 0.001$ (Kruskal-Wallis ANOVA with Mann-Whitney test).

Figure 7. ANO1, TRPV1 and IP$_3$R1s are found in close proximity in small-diameter DRG neurons as tested with STORM. (A-C) Right panels display representative STORM images from DRG neurons, double-labeled for either TRPV1 and ANO1 (A), ANO1 and IP$_3$R1 (B), or TRPV1 and IP$_3$R1 (C) using dye-pairs of Alexa Fluor 405/ Alexa Fluor 647 (green centroids) and Cy3/ Alexa Fluor 647 (red centroids); scale is indicated by the white bars. Scale bars represent: Left panel, 5μm; middle panel, 1μm; right panel, 0.2μm for A-C. **(D to F)** Cluster distributions representing double-labeled TRPV1-ANO1; n=6 neurons (D), ANO1-IP$_3$R1; n=9 neurons (E), or TRPV1-IP$_3$R1; n=6 neurons (F). Summary data for cluster percentages, localization number per cluster, and probability distribution statistics are given in **tables S1-S3**.

Figure 8. Imaging of ANO1-TRPV1-IP$_3$R1s complexes using three-color STORM. (A, B) Representative STORM images for triple-labeled ANO1 (blue centroids) TRPV1 (green centroids) and IP$_3$R1 (red centroids) in DRG neurons; scale is indicated by the white bars. Scale bars represent: A; Left panel, 5 μm; middle panel, 1 μm; right panel, 0.2 μm; B; 0.2 μm for all images. **(C)** Cluster distributions representing triple-labeled ANO1-TRPV1-IP$_3$R1 combinations of proteins, protein pairs, or single

proteins; n=12 neurons. Summary data for cluster percentages, localization number per cluster, and probability distribution statistics are given in **tables S1-3**. **(D)** Schematic depicting possible ANO1-TRPV1-IP$_3$R1 functional coupling in DRG neurons. Our data suggests that a sizable fraction of ANO1, TRPV1 and IP$_3$R1s are in close proximity at the ER-PM junctions and form complexes in small-diameter DRG neurons. TRPV1 activation leads to Na$^+$ and Ca^{2+} influx (middle) but can also activate IP$_3$R Ca^{2+} release (right), presumably through PLC activation. Release of Ca^{2+} from the ER maximizes ANO1 activation (right) which ultimately causes Cl$^-$ efflux and depolarization of the neuron.
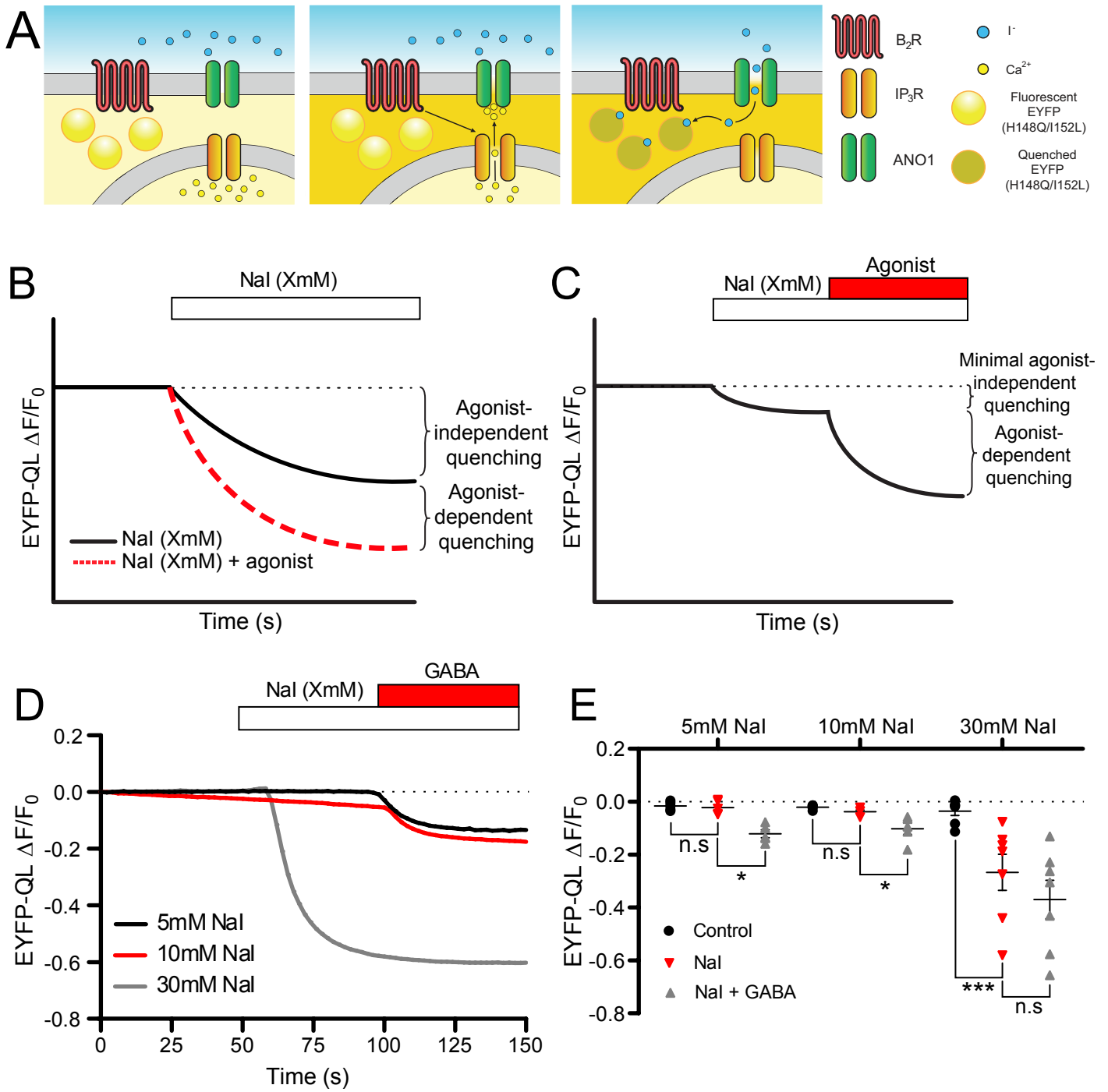
Figure 1
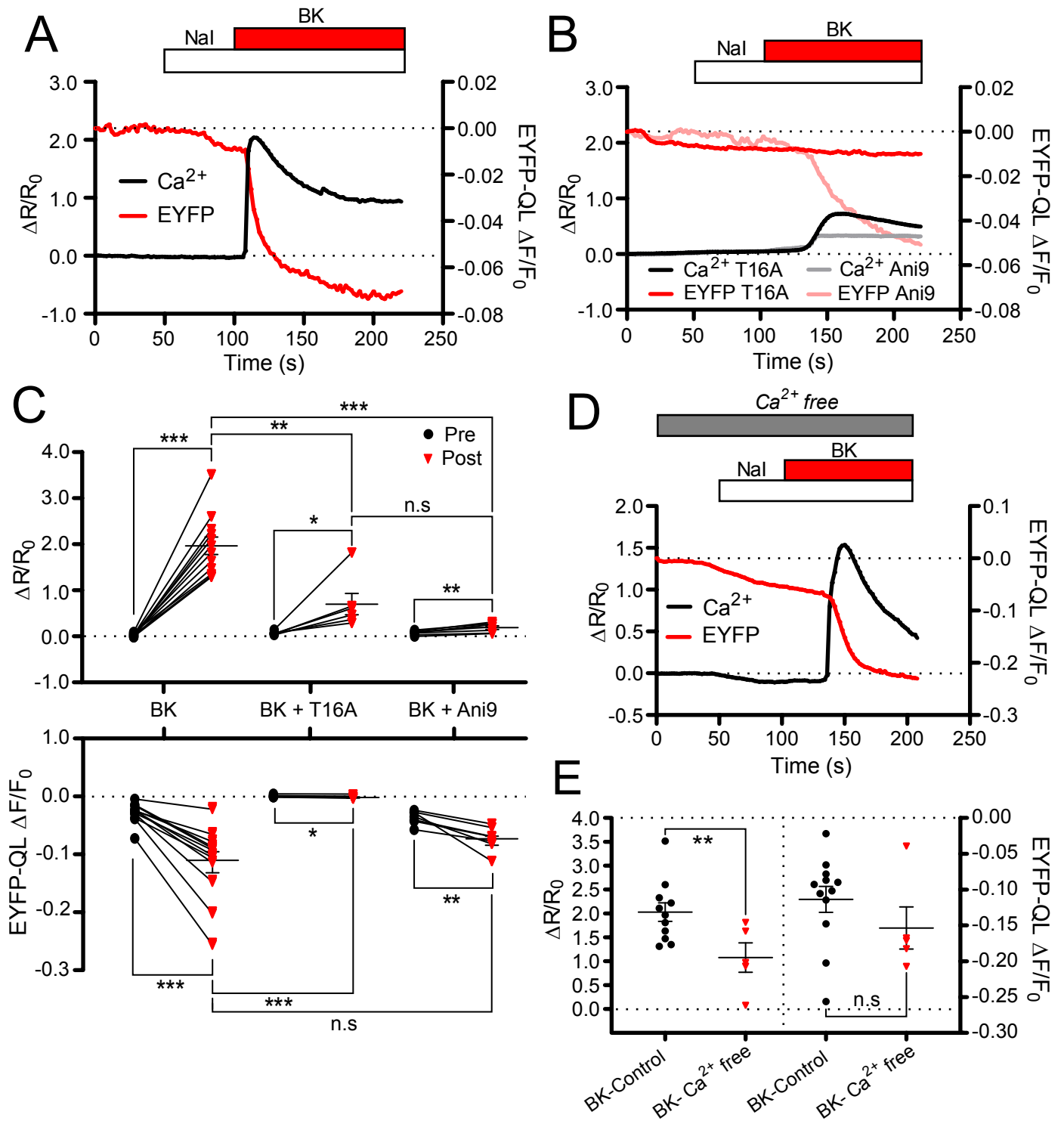
Figure 2
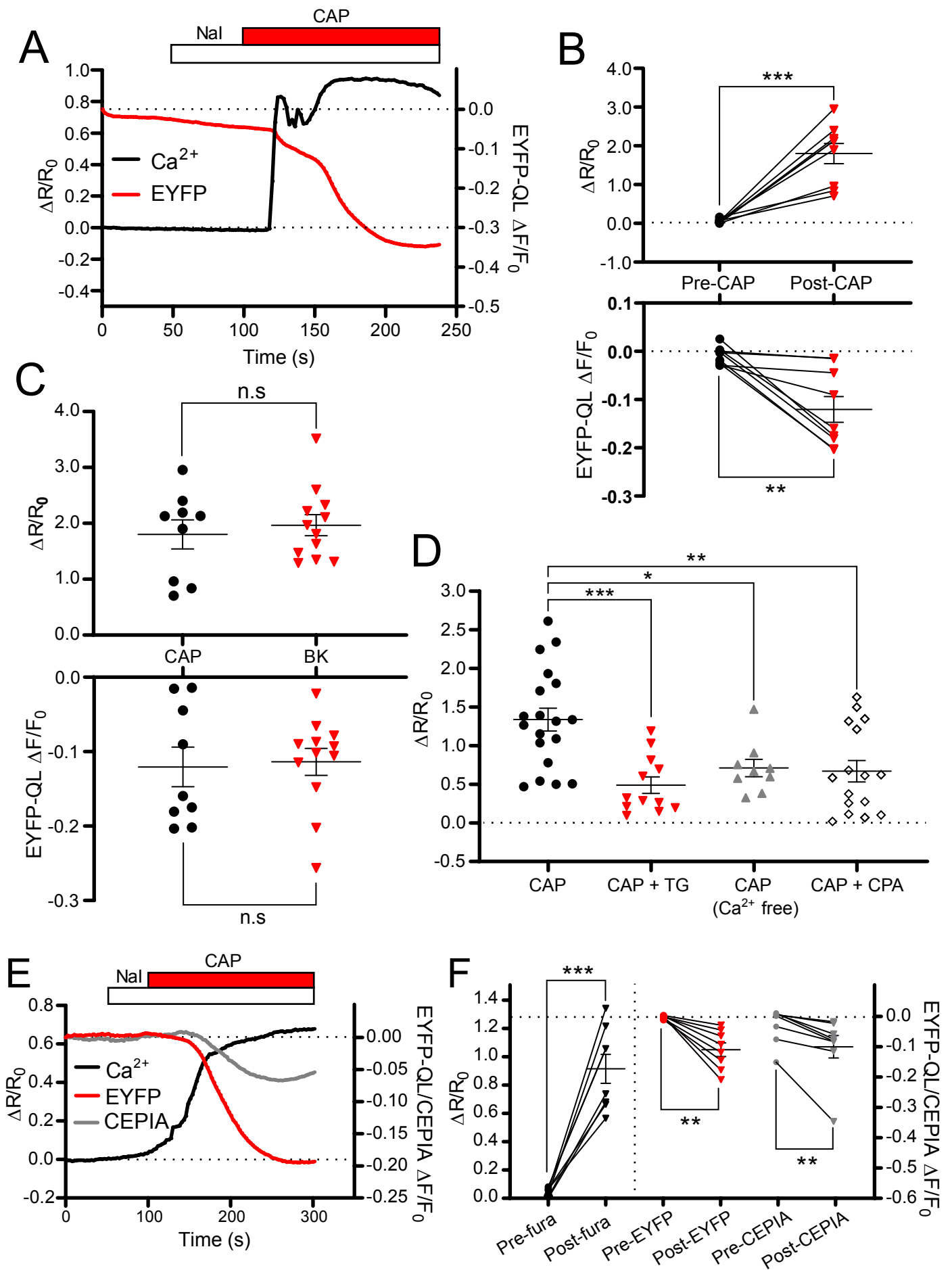
Figure 3

Figure 4

Figure 5

A

BRIGHTFIELD | PLA: TRPV1-ANO1 | MERGE

B

BRIGHTFIELD | PLA: ANO1-IP$_3$R1 | MERGE

C

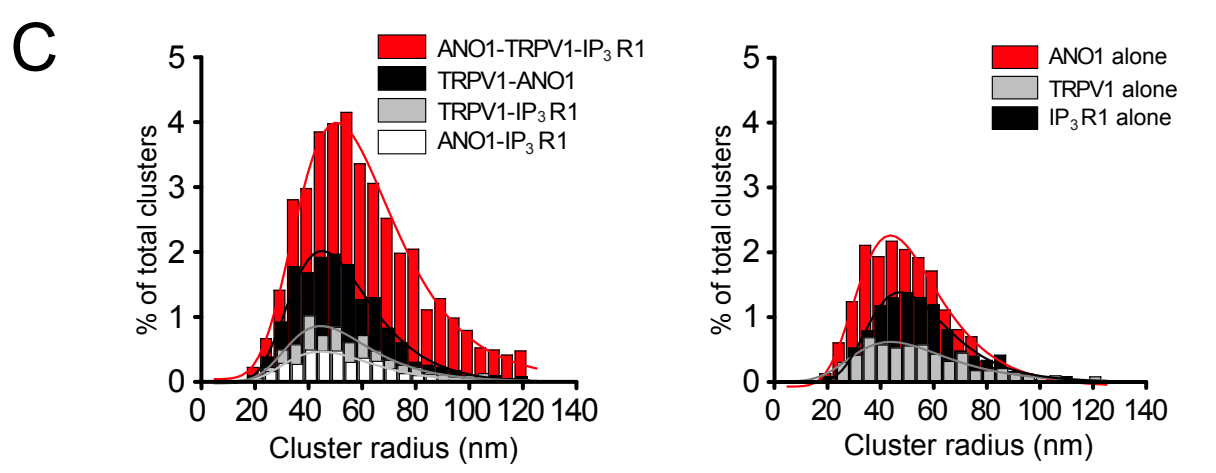BRIGHTFIELD | PLA: TRPV1-IP$_3$R1 | MERGE
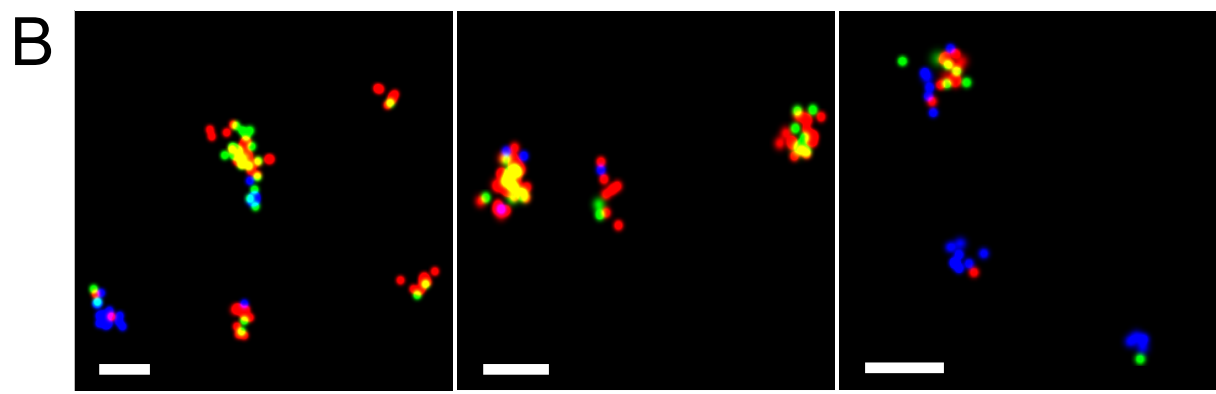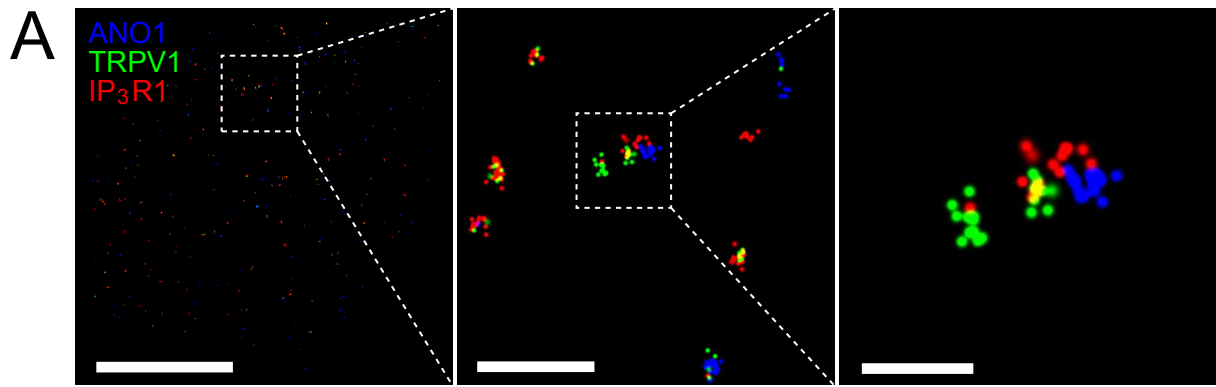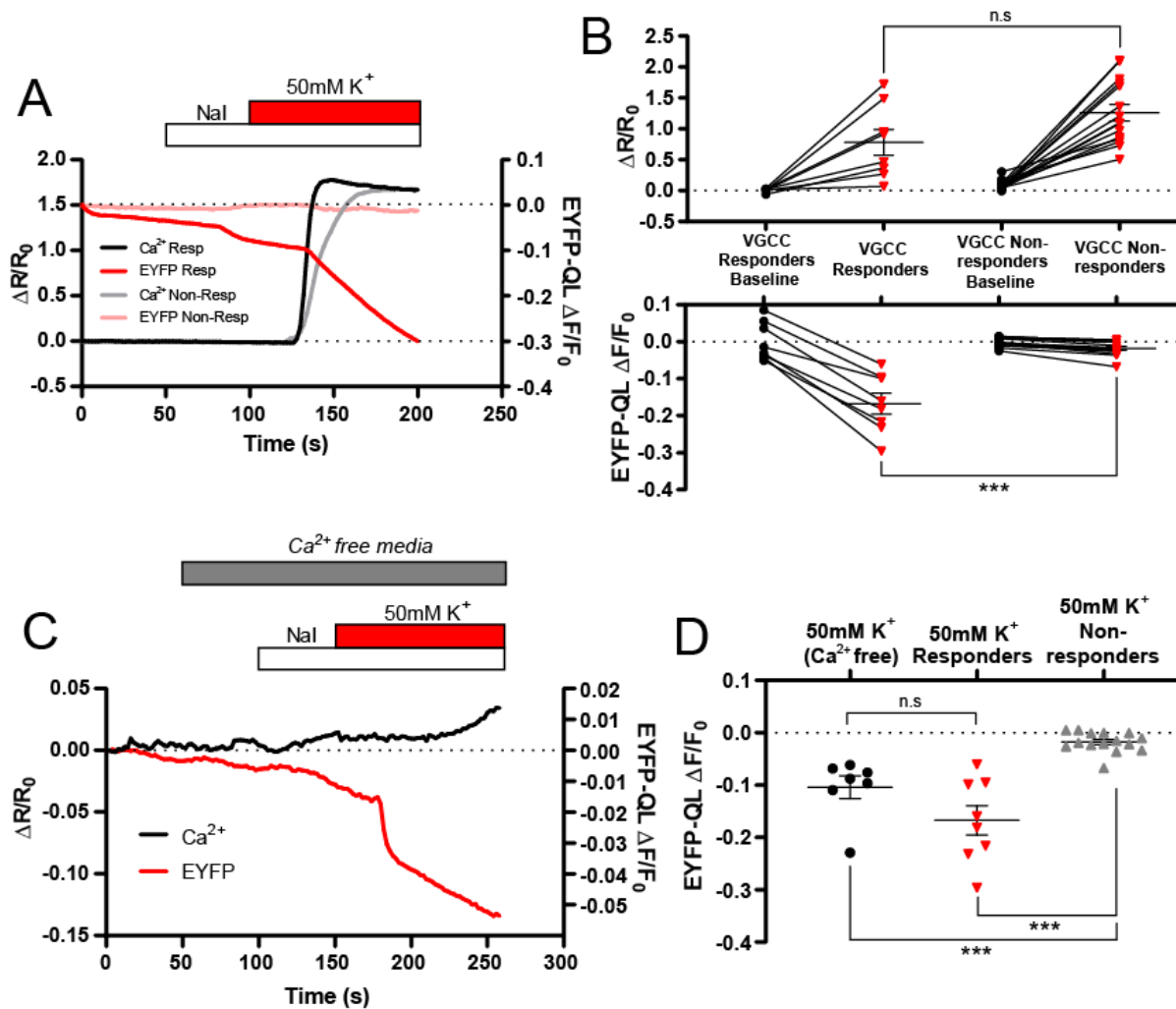
D
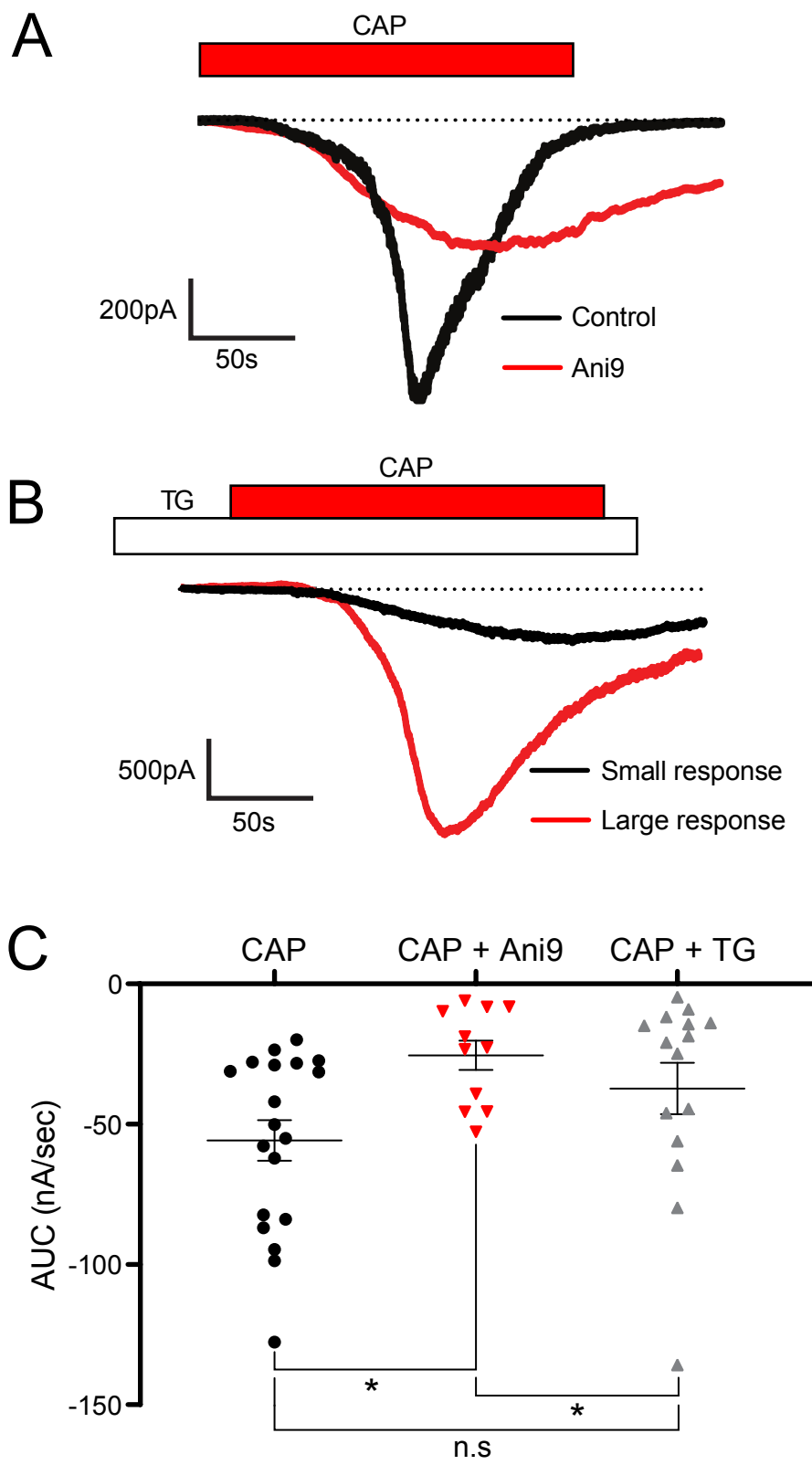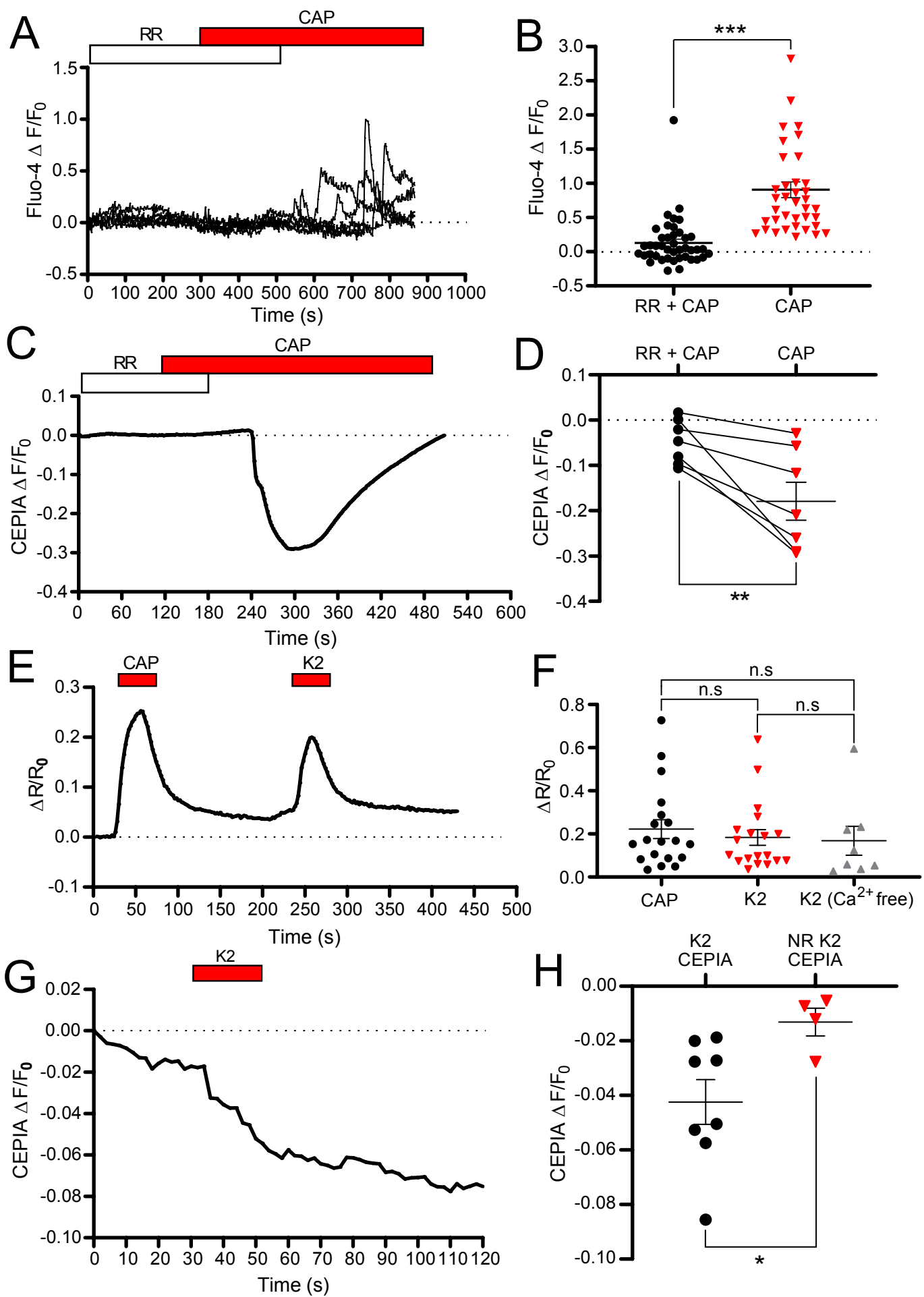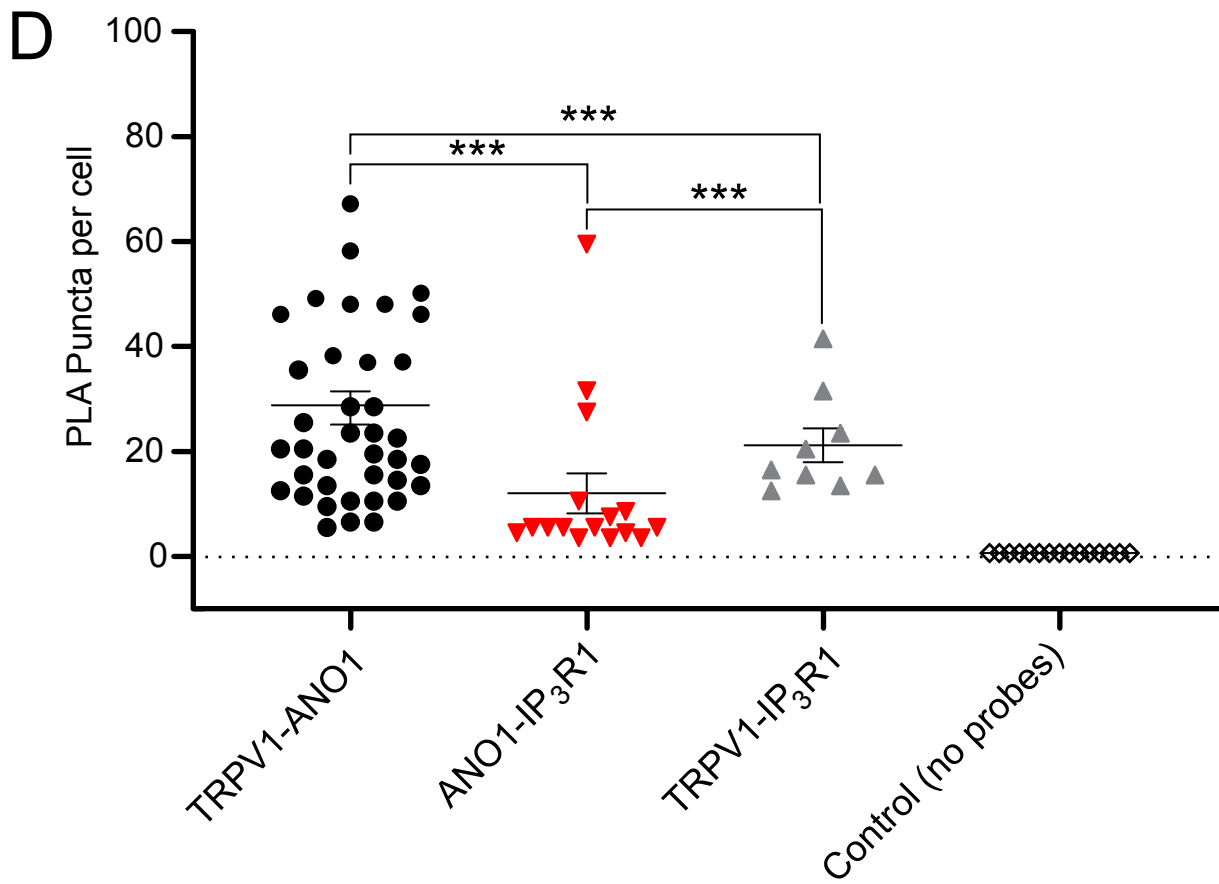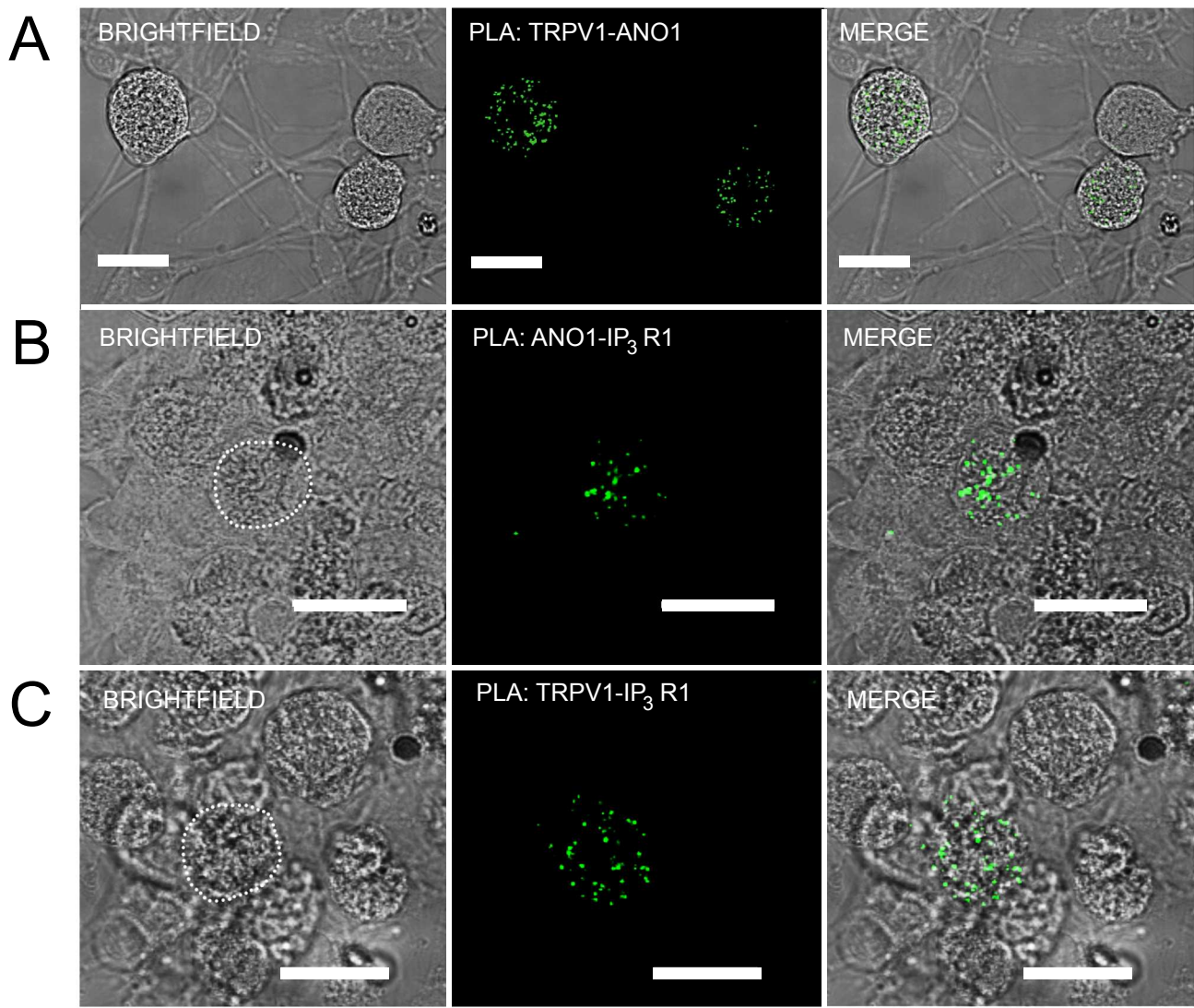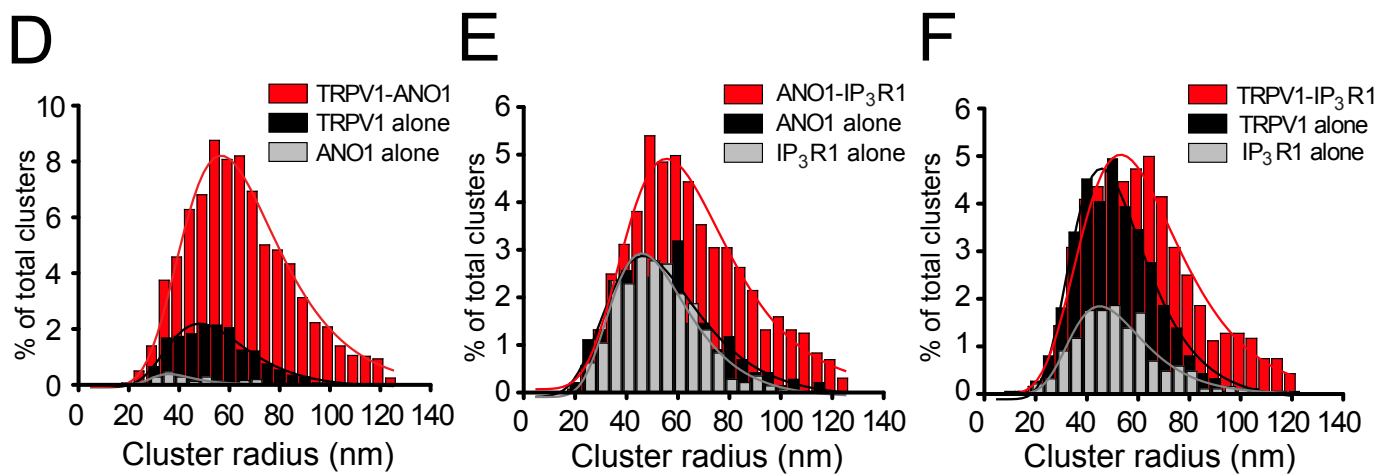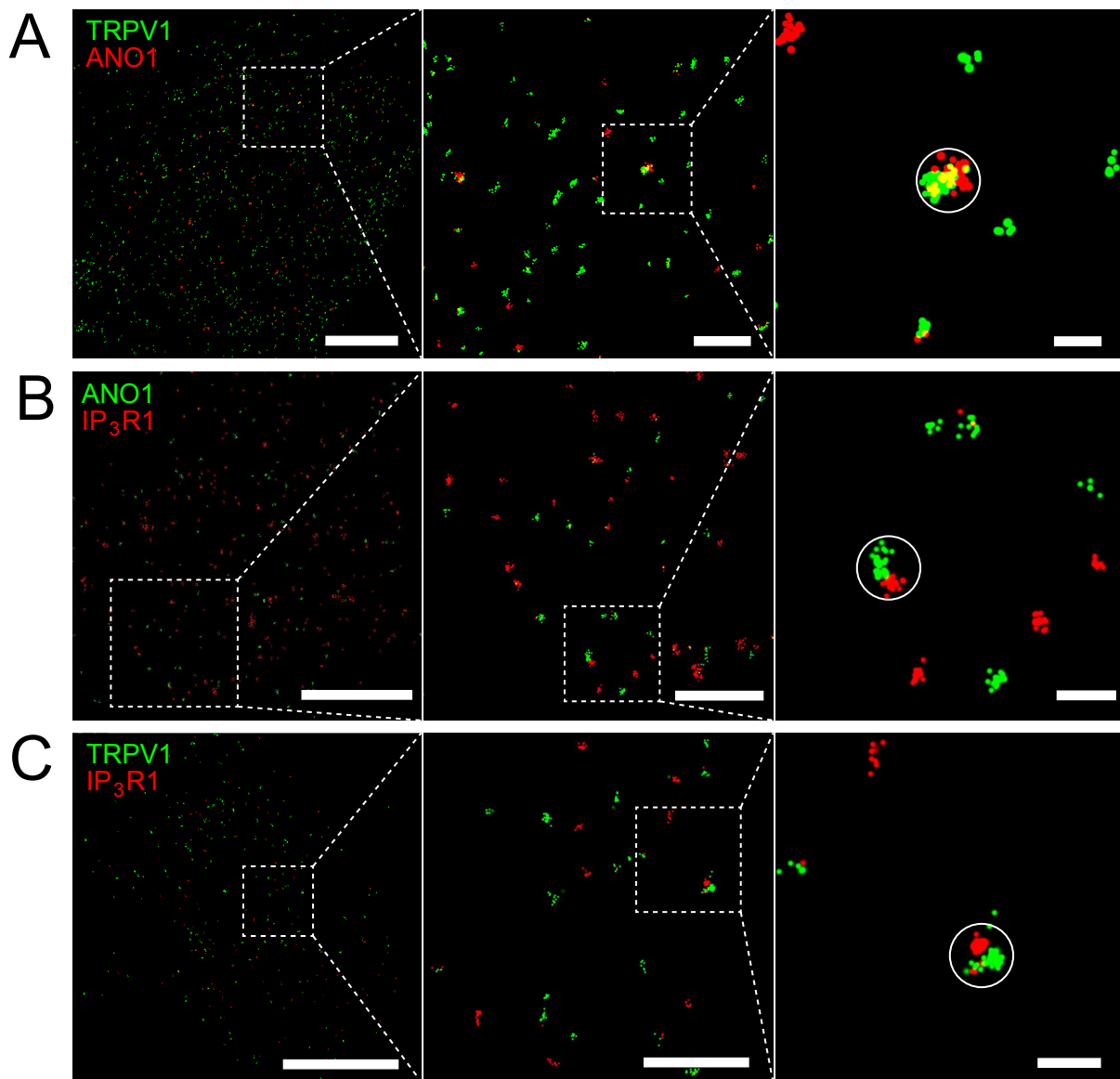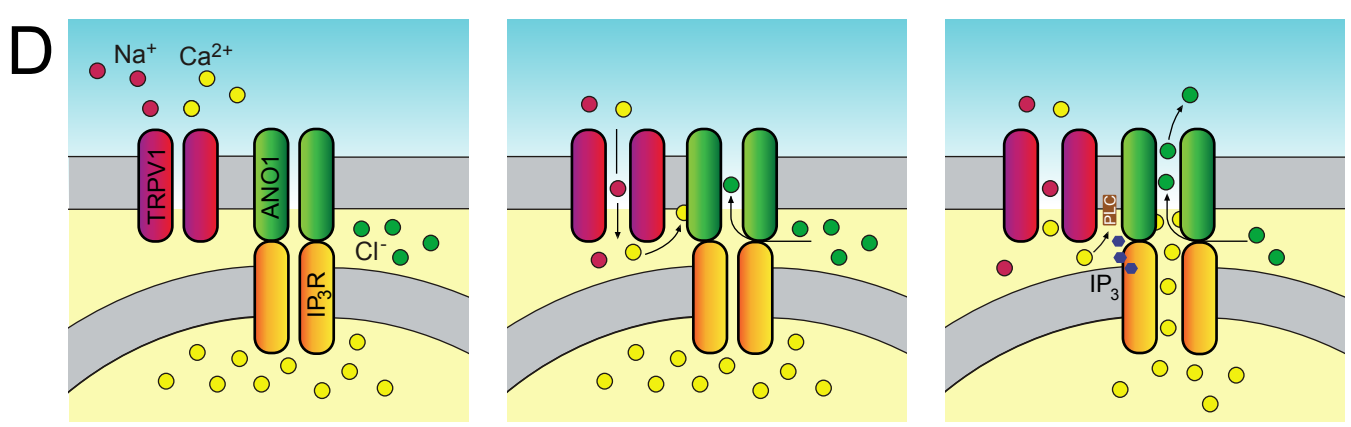
Figure 6

Figure 7

Figure 8

Figure S1. Depolarization-induced I$^-$ influx is a Ca^{2+}-independent phenomenon. (A) Representative traces showing Ca^{2+} rises and a concurrent EYFP-QL fluorescence quenching in small-diameter DRG neurons transfected with EYFP-QL and loaded with fura-2AM in response to depolarization with 'high-K$^+$' (50 mM KCl) extracellular solution. Representative traces for a 'responding' (black and red traces) and 'non-responding' (grey and pink traces) neuron are shown. Subdivision in responding and non-responding neurons is made on the basis of EYFP-QL fluorescence quenching; no response is considered when quenching is less than 5% of the baseline. **(B)** Scatter plots summarizing experiments similar to these shown in (A); n=8 responding neurons, n=13 non-responding neurons. **(C)** Similar to (A) but recordings were performed in Ca^{2+}-free conditions. **(D)** Scatter plots summarizing experiments similar to these shown in (A-C); for the experiment performed in Ca^{2+}-free conditions, n=7 neurons. In B, D, asterisks denote the following: ***p<0.001; n.s, not significant (Kruskal-Wallis ANOVA).

A

Condition

ΔR/R$_0$

— CAP
— CAP + TG
— CAP Ca^{2+} free
— CAP + CPA

Time (s)

B

NaI   CAP/CAP + TG

ΔR/R$_0$

EYFP-QL ΔF/F$_0$

— Ca^{2+} CAP + TG
— EYFP CAP + TG
— Ca^{2+} CAP
— EYFP CAP

Time (s)

C

ΔR/R$_0$

EYFP-QL ΔF/F$_0$

**
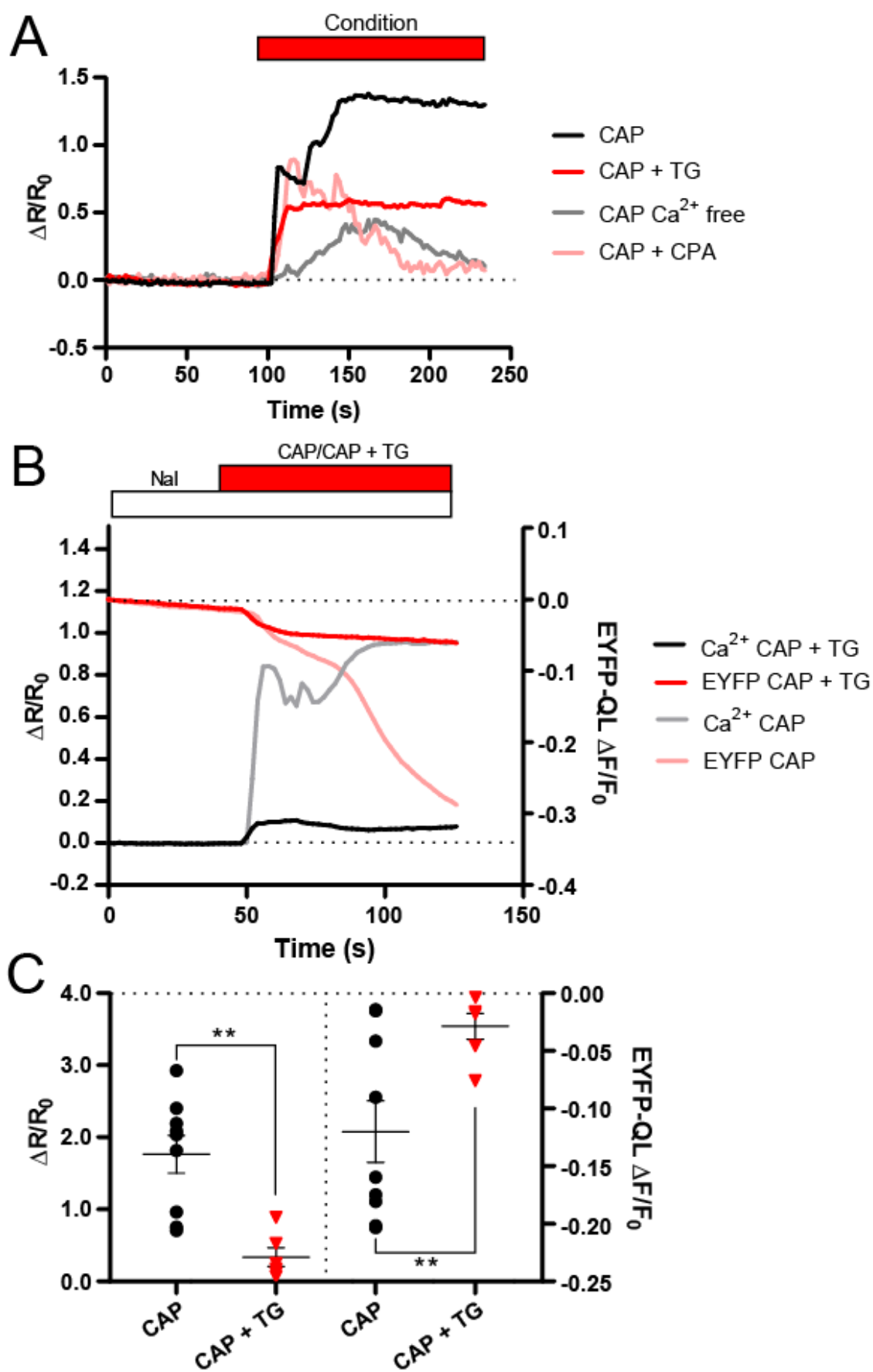
**

CAP   CAP + TG   CAP   CAP + TG

Figure S2. ER Ca²⁺ store depletion severely reduces Ca²⁺ transients and CaCC activation in response to capsaicin. (A) Representative traces showing Ca²⁺ rises in response to capsaicin application under control conditions (black trace), thapsigargin (TG, 1 μM; red trace), Ca²⁺ free conditions (grey trace) or cyclopiazonic acid (CPA, 1 μM; pink trace) in small-diameter DRG loaded with fura-2AM. (B) Representative traces comparing capsaicin-induced Ca²⁺ rises and concurrent EYFP-QL fluorescence quenching in small diameter DRG neurons transfected with EYFP-QL and loaded with fura-2AM in TG (1 μM) pre-treated (black and red traces) and control (grey and pink traces) cells. (C) Summary of the fura-2 and EYFP-QL responses for capsaicin application in control and TG pre-treated neurons; n=6 neurons. **p<0.01 (paired t-test).
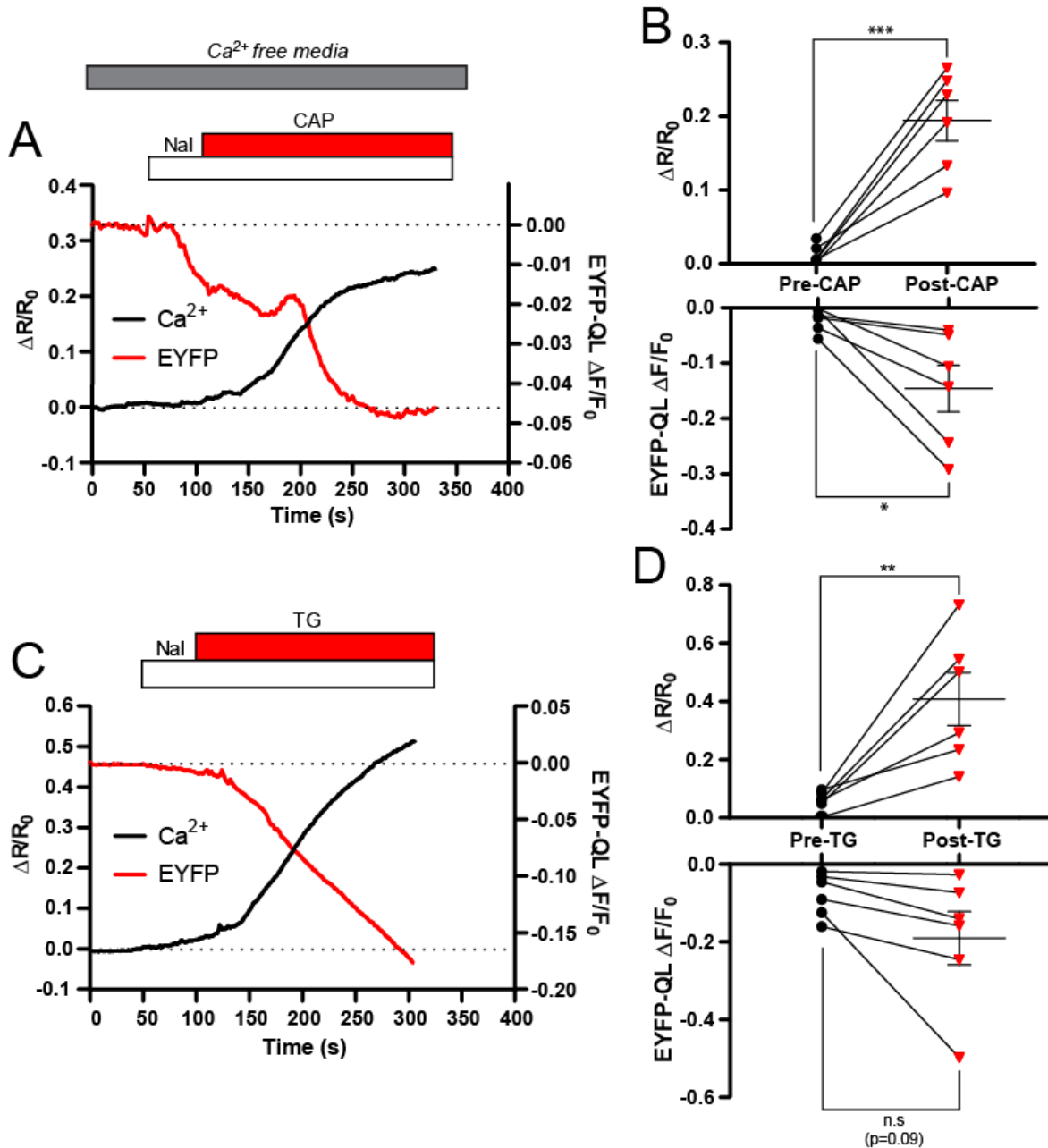

Figure S3. Capsaicin applied in extracellular Ca²⁺-free conditions and acute thapsigargin-induced ER Ca²⁺ leak can induce a degree of CaCC activation. (A)

Representative traces showing a Ca^{2+} rise and a concurrent EYFP-QL fluorescence quenching in a small-diameter DRG neuron transfected with EYFP-QL and loaded with fura-2AM in response to capsaicin (1 μM) application in Ca^{2+}-free extracellular solution. **(B)** Scatter plots summarizing experiments similar to those shown in (A); n=6 neurons. **(C)** Representative traces showing a Ca^{2+} rise and a concurrent EYFP-QL fluorescence quenching in a small-diameter DRG neuron transfected with EYFP-QL and loaded with fura-2AM in response to acute TG (1 μM) application. **(D)** Scatter plots summarizing experiments similar to those shown in (C); n=6 neurons. In B, D, asterisks denote the following: *p<0.05, **p<0.01, ***p<0.001; n.s, not significant (paired t-test).
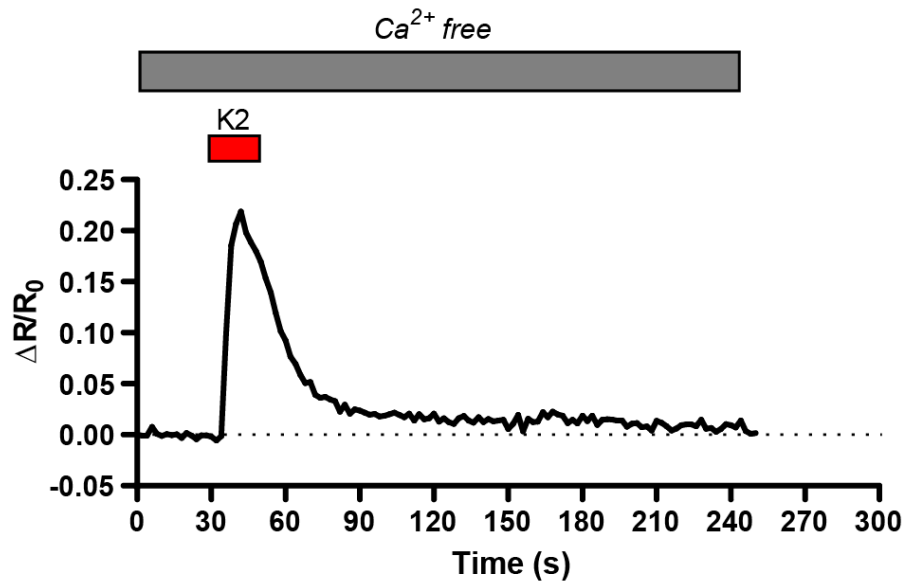

Figure S4. The cell-impermeable TRPV1 agonist K2 evokes cytosolic Ca^{2+} transients in the absence of extracellular Ca^{2+}. Representative trace showing a Ca^{2+} rise in response to K2 (30 μM) application in small-diameter DRG neuron loaded with fura-2AM; n=8 neurons.
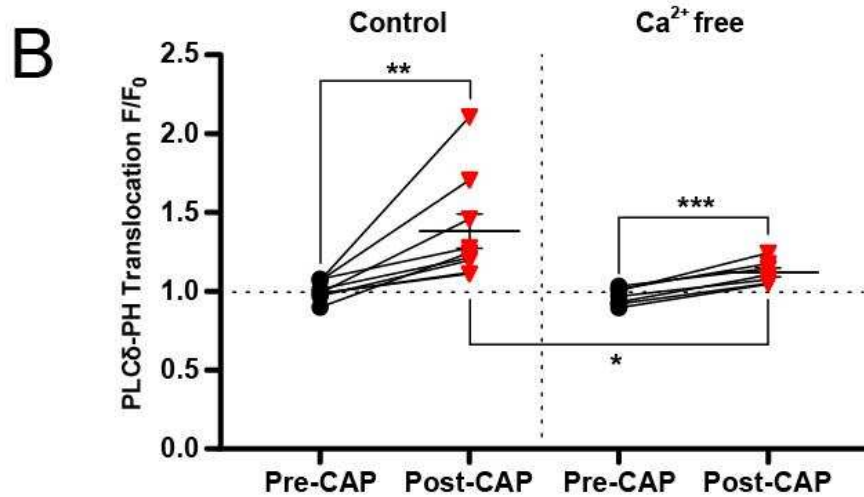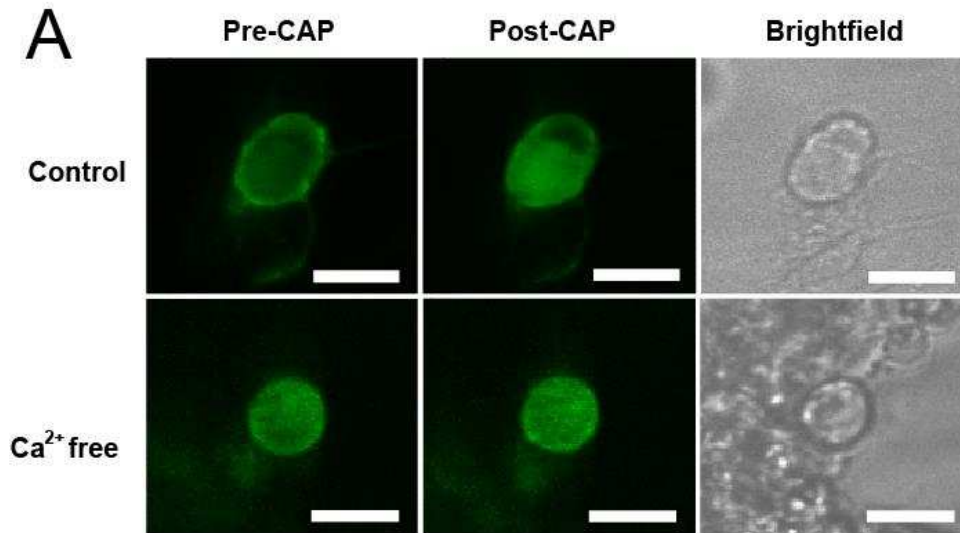
Figure S5. Capsaicin induces PLC activation in DRG neurons. (A) Images of DRG neurons transfected with the optical PIP_2 reporter PLCδ-PH-GFP, before and after capsaicin (1 μm) application. Top row: control; bottom row: extracellular Ca^{2+}-free conditions. Brightfield images of neurons also included (right panels). Scale bars represent 20 μm in all images. **(B)** Scatter plots summarizing changes in cytosolic fluorescence intensity before and after the capsaicin application in experiments similar to these shown in (A); control (n=9 neurons); Ca^{2+}-free (n=7 neurons). F/F_0 was used for analysis. *p<0.05, **p<0.01 and ***p<0.001 (Wilcoxon signed-rank test, paired T-test and Mann-Whitney test).
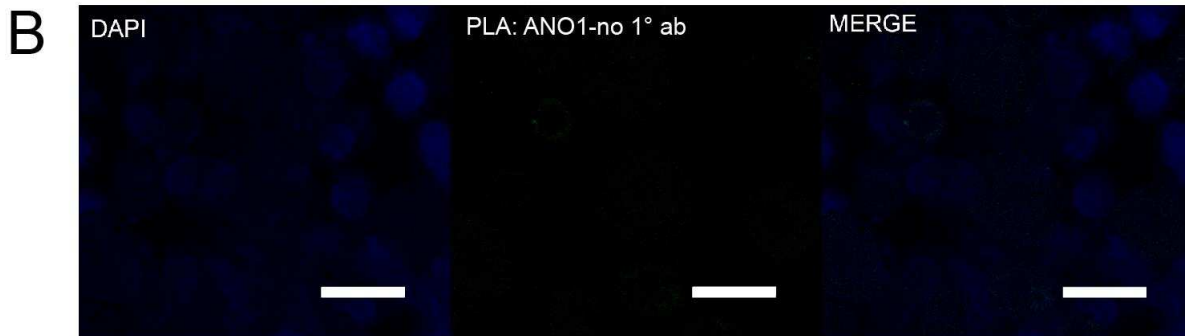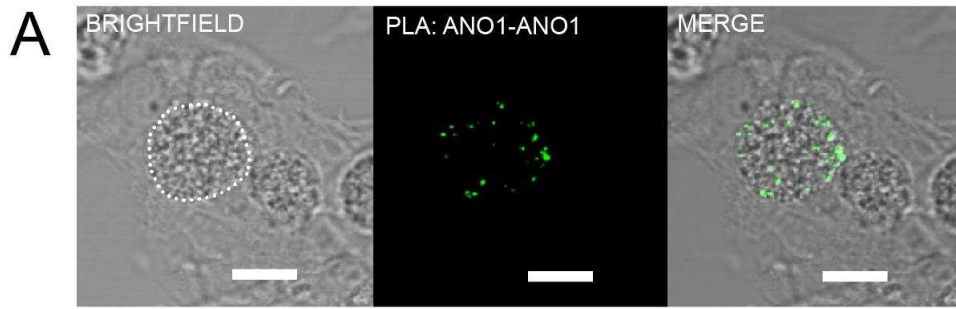
Figure S6. Controls for PLA. (A) Positive control: DRG neurons were stained with 2 primary antibodies (raised in rabbit and goat, respectively) and 2 corresponding secondary PLA probes. Left panel: brightfield image; middle panel: PLA puncta detection; right panel: merged image of brightfield and PLA puncta; n=8 neurons. Scale bars represent 10 μm in all images. **(B)** Negative control: DRG neurons were stained with one primary antibody (anti-ANO1 raised in rabbit) and two secondary PLA probes (anti-rabbit and anti-goat); n=15 neurons. No PLA puncta were detected in these experiments. Scale bars represent 20 μm in all images.
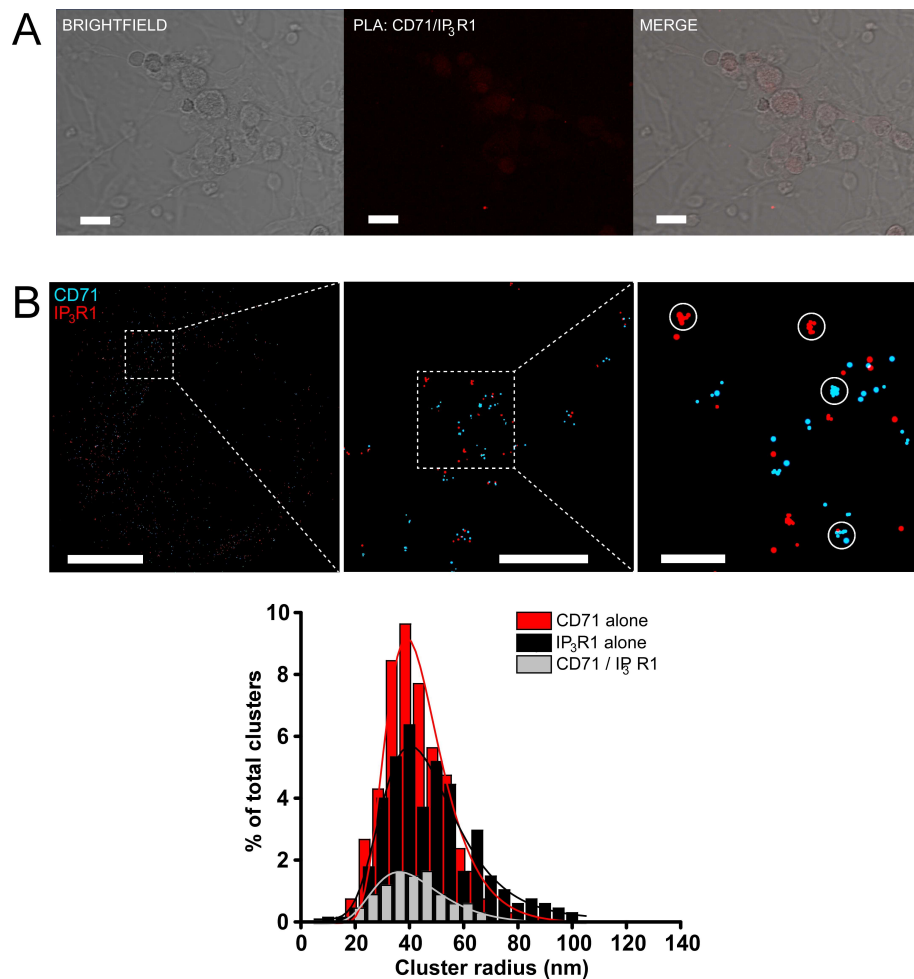
Figure S7. CD71 and IP₃R1 are not found in close proximity as confirmed by PLA and STORM analysis. (A) Images of PLA performed with CD71 and IP₃R1 antibodies; n=17 neurons. Scale bars represent 20 μm in all images. **(B)** Right panel displays representative STORM images from DRG neurons, double-labeled for CD71 and IP₃R1 using dye-pairs of Alexa Fluor 405/ Alexa Fluor 647 (blue centroids) and Cy3/Alexa Fluor 647 (red centroids); Lower graph displays cluster distributions representing CD71 alone, IP₃R1 alone and CD71-IP₃R1 clusters; n=7 neurons. Scale bars represent the following, Left panel: 5 μm; middle panel: 1 μm; right panel: 0.5 μm.
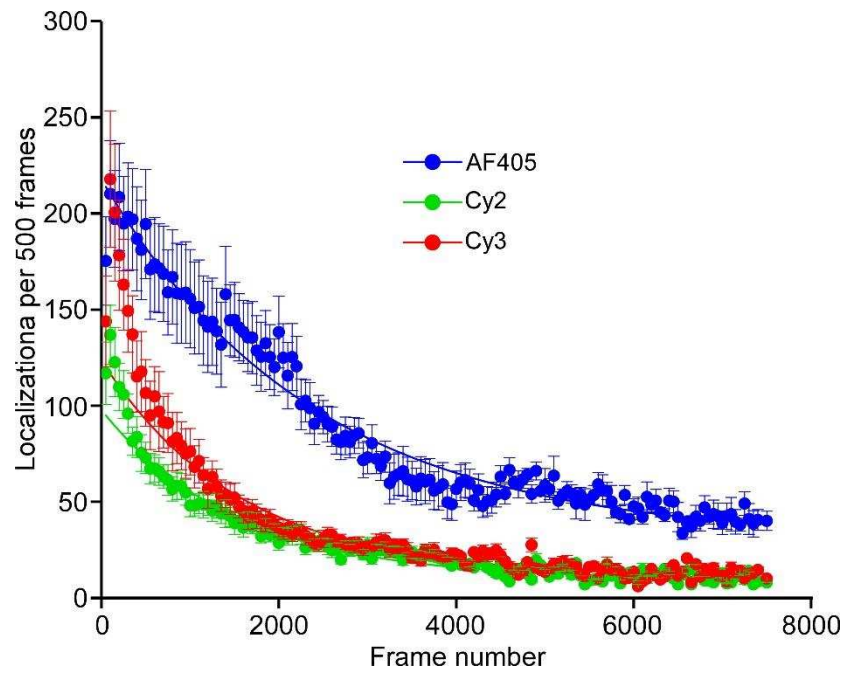
Figure S8. Decay rates of STORM fluorescent dye labels after repeated laser activation cycles. Depicted are the localizations acquired over time under traditional STORM from primary DRG neurons that were fixed and stained with primary antibodies against ANO1 (405), TRPV1 (Cy2), and IP$_3$R1 (Cy3). The dye pairs of Alexa Fluor 405/Alexa Fluor 647 (conjugated to anti-goat IgG), Cy2/Alexa Fluor 647 (conjugated to anti-guinea pig IgG), or Cy3/Alexa Fluor 647 (conjugated to anti-rabbit IgG) were used. Only localizations from the first reporter frame of specific activation were tabulated and binned every 500 frames (each frame=16 ms) according to the time at which they were acquired in STORM. Each dye was fit to a single exponential decay function, $y = y_0 + A \cdot e^{-x/t}$. Data represent mean $\pm$ SEM. n=9 neurons per group.

Table S1. Mean percentages of STORM cluster distributions detected by DBSCAN

Labeling							
TRPV1-ANO1	TRPV1	ANO1	TRPV1+ANO1				
	$23.6 \pm 6.4\%$	$2.2 \pm 0.4\%$	$74.1 \pm 6.5\%*$				
TRPV1-IP$_3$R	TRPV1	IP$_3$R1	TRPV1+IP$_3$R1				
	$34.0 \pm 4.0\%$	$14.1 \pm 0.8\%$	$51.8 \pm 4.0\%*$				
ANO1-IP$_3$R	ANO1	IP$_3$R1	ANO1+IP$_3$R1				
	$23.8 \pm 4.0\%$	$22.0 \pm 8.1\%$	$54.1 \pm 4.3\%\#$				
ANO1-TRPV1-IP$_3$R1	ANO1	TRPV1	IP$_3$R1	TRPV1+ANO1	ANO1+ IP$_3$R1	TRPV1+IP$_3$R1	ANO1+TRPV1+IP$_3$R1
	$17.3 \pm 1.8\%$	$4.7 \pm 1.2\%$	$11.4 \pm 2.7\%$	$15.7 \pm 1.7\%$	$4.2 \pm 0.04\%$	$6.4 \pm 1.7\%$	$40.2 \pm 2.5\%\dagger$

All data values represent mean percentage of total clusters $\pm$ SEM; n=6-12 neurons per labeling group. * $p < 0.05$ compared to TRPV1; # $p<0.05$ compared to ANO1; † $p<0.05$ compared to TRPV1+ANO1.

Table S2. Mean cluster radius sizes of STORM-derived clusters detected by DBSCAN

ANO1-TRPV1-IP$_3$R1	ANO1	TRPV1	IP$_3$R1	TRPV1+ANO1	ANO1+IP$_3$R1	TRPV1+IP$_3$R1	ANO1+TRPV1+IP$_3$R1
Cluster size (nm)	49.2 ± 1.0	52.7 ± 1.9	50.8 ± 1.4	52.7 ± 2.2	51.6 ± 1.8	47.9 ± 1.1	64.2 ± 1.8*
β scale parameter	15.1	17.6	14.5	15.0	15.6	14.8	18.0*

Data represent mean cluster radius size (nm) ± SEM; n=12 neurons per labeling group. The β continuous scale parameter was derived from the combined probability distribution function of all detected clusters of each category. * p< 0.05 compared to TRPV1+ANO1.

Table S3. Mean number of localizations per cluster from STORM-derived clusters detected by DBSCAN

Labeling/parameter							
TRPV1/ANO1	TRPV1	ANO1	TRPV1+ANO1				
Localizations	15.6 ± 0.8	11.2 ± 0.4	23.9 ± 1.2				
TRVP1/ IP$_3$R1	TRPV1	IP$_3$R1	TRPV1+ IP$_3$R1				
Localizations	13.8 ± 0.6	14.1 ± 0.8	20.1 ± 0.7				
ANO1/ IP$_3$R1	ANO1	IP$_3$R1	ANO1+ IP$_3$R1				
Localizations	14.0 ± 0.7	16.7 ± 0.3	24.8 ± 1.9				
ANO1/TRPV1/ IP$_3$R1	ANO1	TRPV1	IP$_3$R1	TRPV1+ANO1	ANO1+IP$_3$R1	TRPV1+IP$_3$R1	ANO1+TRPV1+IP$_3$R1
Localizations	13.8 ± 0.2	15.7 ± 0.9	16.0 ± 0.6	15.0 ± 0.7	13.9 ± 0.6	16.4 ± 0.8	22.1 ± 0.7*

Data represent mean number of localizations per cluster $\pm$ SEM; n=6-12 cells per labeling group. * $p<0.05$ compared to TRPV1+ANO1.